NaCl salts in finite aqueous environments at the fine particle marine aerosol scale

Valérie Vallet, Jonathan Coles, Florent Réal, Houriez Céline, Michel Masella

To cite this version:

Valérie Vallet, Jonathan Coles, Florent Réal, Houriez Céline, Michel Masella. NaCl salts in finite aqueous environments at the fine particle marine aerosol scale. ACS Earth and Space Chemistry, 2022, 6 (6), pp.1612-1626. 10.1021/acsearthspacechem.2c00082 . hal-03360947

HAL Id: hal-03360947
https://hal.science/hal-03360947

Submitted on 26 Nov 2023

NaCl salts in finite aqueous environments at the fine particle marine aerosol scale.

Valérie Vallet,[†] Jonathan Coles,[‡] Florent Réal,[†] Céline Houriez,[¶] and Michel Masella[*,§]

[†] *Univ. Lille, CNRS, UMR 8523 - PhLAM - Physique des Lasers Atomes et Molécules, F-59000 Lille, France*

[‡] *Leibniz Supercomputing Centre of the Bavarian Academy of Sciences and Humanities (LRZ), Garching b. München, Germany*

[¶] *MINES ParisTech, PSL Research University, CTP - Centre Thermodynamique des Procédés, 35 rue Saint-Honoré, 77300 Fontainebleau, France*

[§] *Laboratoire Bioénergétique, Métalloprotéines et Stress, Service de Bioénergétique, Biologie Structurale et Mécanismes, Institut Joliot, CEA Saclay, F-91191 Gif sur Yvette Cedex, France*

E-mail: michel.masella@cea.fr

Abstract

We investigated isolated sodium/chloride aqueous droplets at the microscopic level, which comprise from about 5k to 1M water molecules and whose salt concentrations are $0.2m$ (brackish water) and $0.6m$ (sea water), by means of molecular dynamics simulations based on an *ab initio*-based polarizable force field. The size of our largest droplets is at the submicron particle marine aerosol scale. From our simulations, we investigated ion spatial distributions, ion aggregates (size, composition, lifetime and distribution), droplet surface potentials and the densities of the water vapor surrounding the droplets. Regarding ions, they form a weak electrostatic double layer extending from the droplet boundary to 2 nm within the droplet interior. Free Na^+ and ion aggregates are more repelled from the boundary than free Cl^-. Most of the droplet properties depend on the droplet radius R according to the standard formula $A = A_\infty(1 - 2\delta/R)$, where A_∞ is the bulk magnitude of the quantity A and δ is a length at most at the nm scale. Regarding the water vapor densities they obey a Kelvin relation corresponding to a surface tension whose Tolman length is negative and at the 1 nm scale. That length is about one order of magnitude larger than for pure water droplets, however it is weak enough to support the reliability of a standard Kelvin term (based on planar interface surface tensions and water densities) and of the related Kölher equation to model sub-micron salty aerosols.

1 Introduction

Molecular scale phenomena at water/vapor interfaces are at the origin of strong modulation of many chemical reactions as compared to bulk.[1–3] They are key factors to understand a large variety of important effects from enzyme catalysis[4,5] to corrosion[6] and they are thus of fundamental importance in atmospheric science. Besides their role in pollution effects,[7] their role in atmospheric absorbing/scattering solar radiation as well as in cloud condensation[8] and ice formation[9] explain their importance to understand and model climate change.[10]

Oceans are the main contributors of water aerosols (termed as Sea Spray Aerosols, SSAs) with radii that typically range from the 0.01 to the 10 μm scale.[11–14] Fresh large SSAs (at the micron scale and above) are composed of unaltered sea water (a brine of sodium/chloride and magnesium sulfate salts that can also be enriched microorganisms[15]) whereas sub-micron SSAs can be enriched by organic compounds (like fatty acids and sugars) compared to bulk sea water. Size distributions of SSAs depend on their location on earth. The diameters of the most abundant SSAs vary from 20 to 200 nm as reported by surface level measurements.[16] In particular fine SSAs (at the 20 nm diameter scale) are reported to be the most abundant in marine boundary layers of the Southern Pacific[17] and North Atlantic[18] oceans.

As bulk systems, experimental and theoretical investigations of SSA properties, like the spatial distribution of their different components, double-layer formations, orientational and inter species cooperative effects, are highly challenging and still poorly documented, as recently reviewed by Björnehom and co-workers.[19] Molecular dynamics, MD, numerical simulations are now widely used to investigate the microscopic properties of any kind of molecular systems. With the ongoing increase of the available computational resources, MD simulations of relatively large bulk molecular systems are now routinely performed, in particular to investigate microscopic phenomena at liquid water (planar) interfaces, see among others Refs. [20–29].

The main difficulty that MD simulations face concerns the accuracy of the potential energy terms (the force field for classical MD) that are used to model microscopic forces. The parameters of most of the available force fields, in particular those used to simulate salty aqueous systems, are adjusted to reproduce experimental data, like osmotic pressures.[30,31] Besides the force-field sophistication (like accounting explicitly for microscopic polarization), the latter strategy to build force fields gives rise questions about their transferability, *i.e.* their ability to accurately describe molecular systems in physical states that were not considered to adjust them. To tackle these difficulties, new classes of force fields, termed *ab initio*-based force fields and whose parameters are adjusted only by considering *ab initio* quantum chemistry data regarding small molecular systems,[32] are inferred to be potentially more accurate and to allow investigations of molecular systems for which no experimental data are available.

As all the studies mentioned above, most of the available MD simulations of salty aqueous solution/gas phase boundaries regard planar interfaces simulated using periodic boundary conditions. The size of the simulation boxes are overall small: they typically comprise from 2000 to 10 000 water molecules and ions. Nevertheless they are shown to provide reliable data regarding the properties of planar interfaces and thus, as usually inferred, of spherical interfaces corresponding to large enough finite size molecular systems, at the 10^6 molecules scale and above.[33] Assuming the water density within SSAs to match the liquid water one (33.3 molecules nm^{-3} at ambient conditions), the radius of a SSA comprising 10^6 molecules is about 20 nm. From the size distributions of SSAs mentioned above, simulations of planar interfaces are thus well suited to investigate the properties of a sizable part of the SSAs but not of the finest ones that are far from being negligible and that may even be the most abundant at ocean surface levels.

Moreover there are still controversies about the reliability of all the laws related to the Gibbs classical thermodynamic framework of interfaces (*i.e.* interfaces that correspond to large surfaces separated by thin boundary layers) to model sub-micron SSAs, as recently discussed in Refs.[34–37] (see also the references cited therein). Among these laws, we may cite the Tolman relation to compute the surface tension of spherical finite droplets,[38] a key parameter of the Köhler equation to quantify the ability of a SSA to evolve towards a cloud condensation nucleus.[16,39]

Regarding liquid-like finite size systems and besides Functional Density approaches,[40,41] only one component homogenous systems, like pure aqueous small droplets[42–44] (up to the 10^4 molecules scale) and pure Lennard-Jones fluids[45,46] (up to the 10^6 molecules scale), have been investigated by means of microscopic simulations to address the above issue regarding the reliability of the laws related to the Gibbs framework. Interestingly and in agreement with recent experiments regarding *n*-propane,[47] the latter simulation studies concluded to the reliability of such laws, even to model water aggregates comprising only a few hundred molecules.[43]

Our aim here is to discuss the ability of the following simple equation to model any property A of quasi-spherical sub-micron SSAs whose radius is R :

$$A(R) \approx A_\infty(1 - \frac{2\delta_A}{R}) + O(\frac{1}{R^2}), \tag{1}$$

here $A(R)$ and A_∞ are the numerical quantities measuring the magnitude of the property A for spherical and planar interfaces, respectively, and δ_A is a length. Note that, for large enough radius R, we may readily rewrite the Tolman relation to match the above equation.

To this end we present MD simulations at ambient temperature of ideal fine SSAs (a brine comprising only NaCl salt) whose molecular size varies from about 5.10^3 (5k) up to 10^6 (1M) water molecules. The simulations were performed by means of the latest version of our *ab initio*-based polarizable force field.[48–51] We focus our discussions on properties like surface potential, ion distribution and ion clustering. To assess the accuracy of our simulation protocol, we systematically extrapolate bulk quantities from our salty SSA data and we compare them to available experimental and simulation results regarding planar interfaces of salty solutions. Lastly, we also discuss water densities in the vapor phase surrounding our SSAs, which allows us to discuss the reliability of the Kelvin relation, a key component of the Köhler equation, for salty droplets at the sub-micron scale.

Because of the size of our largest droplets (at the 1M molecules scale) and to further assess our simulation protocol, we not only consider systems corresponding to a salt concentration of $0.6m$ (as sea water) but also of $0.2m$. Besides to investigate properties of SSAs originating from brackish waters, simulations of large $0.2m$ systems will provide new insights regarding weakly concentrated NaCl solutions (like ion clustering) that are usually not investigated using standard MD protocols that focused on molar and above salt solutions (see the studies mentioned above). Note that $0.6m$ salty droplets correspond to fresh marine SSAs, whereas aged SSAs evolve towards more concentrated salt systems in the atmosphere.[14]

Lastly, as discussed by Debiec et al.[52] for instance, the Potential of Mean Force, PMF, corresponding to an ion pair dissolved in neat water is an important parameter to assess the reliability of force fields devoted to investigate salt hydration. We will thus also discuss the PMF in bulk water of a single Na^+/Cl^-pair computed from our force fields at ambient conditions by comparing its main features to the predictions of well-accepted theoretical approaches.

2 Theoretical details

2.1 Modeling ion/water interactions

To model hydrated sodium/chloride salts, we consider our own *all-atom* polarizable force fields based on a rigid water representation and for which the total potential energy U is decomposed in five terms

$$U = U^{rep} + U^{qq'} + U^{pol} + U^{coop} + U^{sc}. \tag{2}$$

The first two terms correspond to short-range repulsion and Coulombic interactions

$$U^{rep} = \sum_{i=1}^{N}\sum_{j>i}^{N^*} A_{ij} \exp\left(-B_{ij} r_{ij}\right),$$
$$U^{qq'} = \sum_{i=1}^{N}\sum_{j>i}^{N^*} \frac{q_i q_j}{4\pi\varepsilon_0 r_{ij}}.$$

Here r_{ij} is the distance between the pair of atoms (i,j), q_i are the static charges located on the atomic center i, and A_{ij} and B_{ij} are adjustable parameters. N is the total number of atoms within the molecular system and the superscript * indicates that the corresponding sum does not account analytically for water intramolecular interactions. The polarization term U^{pol} is based on an induced dipole moment approach. The induced dipole moments $\{\mathbf{p}_i\}_{1\leq i\leq N_\mu}$, one per non-hydrogen atom/ion, obey

$$\mathbf{p}_i = \alpha_i \cdot \left(\mathbf{E}_i^q + \sum_{j=1}^{N_\mu^*} \mathbf{T}_{ij} \cdot \mathbf{p}_j\right). \tag{3}$$

The static charge electric field $\mathbf{E}_i^q$ acting on a polarizable atom i is generated by the above charges q_i. α_i is the isotropic polarizability of water and ions, and $\mathbf{T}_{ij}$ is the dipolar interaction tensor. Both $\mathbf{E}_i^q$ and $\mathbf{T}_{ij}$ include short-range Thole-like damping functions.[53] The set of Eqs. (3) is iteratively solved and the resulting polarization energy is

$$U^{pol} = \frac{1}{2}\sum_{i=1}^{N_\mu} \frac{\mathbf{p}_i^2}{\alpha_i} - \sum_{i=1}^{N_\mu} \mathbf{p}_i \cdot \mathbf{E}_i^q - \frac{1}{2}\sum_{i=1}^{N_\mu}\sum_{j=1}^{N_\mu^*} \mathbf{p}_i \mathbf{T}_{ij} \mathbf{p}_j. \tag{4}$$

To accurately model cooperative effects occurring in water hydrogen bond networks and to account for particular electronic density reorganization effects between the water molecules and halide anions, our force fields include a set of short-range cooperative energy terms denoted U^{coop}[48,54,55]

$$U^{coop} = \sum D_e^* f(r) g(\{\theta\}). \tag{5}$$

The sum runs on water/water and water/chloride hydrogen bonds, HBs, r is the HB length and f is a Gaussian function. $\{\theta\}$ is a set of angles allowing one to model the directionality of HBs and the corresponding function g is a product of Gaussian functions of these angles. The originality of our U^{coop} term arises from D_e^* that is not a static parameter: its magnitude is modulated by the chemical environment of the entities involved of a specific HB (precisely by the local density of water molecules at the vicinity of those entities).[48,54,55]

Our force-field parameters to model the hydration of anions and cations are assigned to reproduce quantum *ab initio* data regarding relatively small $[\mathrm{X}^-, (\mathrm{H_2O})_n]$ clusters ($n \leq 6$). For that purpose we only consider quantum data from the MP2 level of theory extrapolated to the Complete Basis Set, CBS, limit. Lastly, we further improve the reliability of our force fields to accurately model large anion/water clusters ($n > 6$ and for which all the water molecules lie in the anion first hydration shell) and alkali cation/water clusters presenting a partial or complete second hydration shell by means of short range many-body functions U^{sc}, whose analytical form is close to the U^{coop}[50,51] (see also the details provided as Supporting Information). For the present purpose, we used the U^{sc} functions (and their parameters) allowing one to model the hydration of Na^+ and Cl^- from our earlier studies.[50,51]

Regarding the full series of halides (from F^- to At^-), we showed the ability of our force fields to reproduce their structural (like anion/water first coordination shell), energetic (hydration enthalpy and Gibbs free energy) and temporal (ion coefficient of diffusion) properties in neat water at ambient conditions.[49–51] In particular our force fields do not yield over polarization effect regarding halides[54] contrary to the present version of the AMOEBA approach,[56] another promising class of polarizable force fields. We have also shown the ability of our force field to model structural and energetic properties regarding cations Li^+, K^+ and NH_4^+ and of its methylated forms.[51,57] Regarding Na^+, we provide new data regarding to its hydration structural properties as computed from our droplet simulations in Supporting Information. These data are in line with experiment.[58]

2.2 The force field to model Na^+/Cl^- interactions

Inter ionic Na^+/Cl^- interactions are modeled by considering only the three energy terms U^{rep}, $U^{qq'}$, U^{pol} detailed above. We assigned the repulsion A_{Na^+,Cl^-} and B_{Na^+,Cl^-} and polarization damping parameters to best reproduce quantum MP2/CBS data corresponding to inter ionic distances ranging from 0.2 to 0.7 nm, namely the ion pair interaction energies and the ion pair total dipole moments. Here CBS data are extrapolated from quantum computations at the MP2 level using the aug-cc-pVXZ (X=T,Q and 5) basis sets and performed using the MOLPRO package of programs.[59,60]

We compare in Figure S3 of Supporting Information the interaction energies of the neutral dimer $[Na^+, Cl^-]$ and of the hetero charged trimers $[(Na^+)_2, Cl^-]$ and $[Na^+, (Cl^-)_2]$ from our force field and quantum computations. A 0.5 % agreement is achieved. That represents an absolute error weaker than 0.5 (dimer) and 1 (trimer) kcal mol^{-1} regardless of the ion distance separation. Regarding the $[Na^+, Cl^-]$ dipole, a similar force-field/quantum agreement is also achieved on average. Even if that does not prejudge of the force-field quality in modeling larger $[Na^+, Cl^-]$ ionic clusters, the latter results support the overall accuracy of our modeling approach.

2.3 Molecular Dynamics details

MD simulations are performed at 300 K in the NVT ensemble using the code POLARIS(MD).[61] All the covalent O−H bonds and H−O−H angles are constrained to their force-field reference values by means of the iterative RATTLE procedure (the convergence criterion is set to 10^{-7} nm). Induced dipole moments are iteratively solved until the mean difference in these dipoles between two successive iterations is less than 10^{-6} Debye. The Newtonian equations of motion are solved using a multiple-time-steps algorithm.[62] From preparatory runs, a reasonable total energy drift is observed along MD trajectories using a time step of 2 fs for intermolecular short-range interactions (corresponding to a cutoff distance of 0.8 nm) and a time step of 6 fs to account for the remaining intermolecular long-range interactions (see Figure S4 of Supporting Information). These time steps are systematically used for our study. Lastly, the system temperature is monitored using the General Gaussian Thermostats.[63]

We compute the Coulombic and polarization energies using a Fast Multipole Method, FMM, scheme devoted to induced dipole-based polarizable force fields.[64] Here we set the FMM opening angle and the multipole expansion order to 0.7 and 7, respectively. As our FMM scheme does not conserve the system total angular momentum, we periodically rescale it so that the kinetic temperature corresponding to the global system rotational degrees of freedom is smaller than 1 K.

To model droplets in equilibrium with a vapor phase, we embedded them in a spherical cavity whose radius R_{cavity} corresponds to half the largest inter atomic distance within the simulation starting structures to which the distance $d = 1.2$ nm is added. The cavity center is set to droplet Center Of Mass, COM. As a water molecule crosses the cavity boundaries it undergoes the harmonic potential $U^{\text{cavity}} = k_{\text{cavity}}(r - R_{\text{cavity}})^2$ for $r \geq R_{\text{cavity}}$ (and $U^{\text{cavity}} \equiv 0$ otherwise). r is the distance between COM and the water oxygen, and k_{cavity} is set to 100 kcal mol^{-1} Å^{-2}. The starting structures correspond to water molecules and ions set on the nodes of a cubic grid (the distance among the nodes is 0.35 nm). During the early simulation stages, these structures evolve towards spherical droplets whose surface is located from 2 (5-10k) up to 5 (1M) nm from the cavity boundary.

We computed the Potential of Mean Force, PMF, using a standard Umbrella Sampling approach of a single $[\text{Na}^+, \text{Cl}^-]$ pair dissolved a cubic box comprising 1000 water molecules using periodic boundary conditions. Coulombic and polarization interactions are computed according to a Smooth Particle Mesh Ewald scheme[65] (the direct term energy cut off and the grid dimension are set to 1.2 and 0.1, and the interpolation order is 8). The details of the Umbrella Sampling approach may be found in our earlier studies (see Ref. 66 for instance).

The MD trajectories are sampled each 10 ps once an initial relaxation phase of 10 ns is achieved. When not detailed, the error regarding the averages discussed below are computed from a basic block analysis scheme. For 10k and 100k droplets, we compute averaged quantities over 10 ns MD segments and we assume the error to be the standard deviation corresponding to those averages. For 1M droplets, we perform the analysis on 5 ns blocks.

2.4 The hydrated NaCl salts simulated

We simulated two sets of NaCl/water droplets corresponding to salt concentrations of 0.2 and 0.6m and comprising from about 5k to 1M water molecules at the 200 ns scale (5k-10k), 100 ns scale (20k-100k) and 30 ns (1M). The largest 1M droplets comprise 4k and 10k $[\mathrm{Na}^+, \mathrm{Cl}^-]$ pairs, respectively, see also a simulation snapshot of the 1M 0.6m water droplet shown in Figure 1.

We also simulated smaller salty 0.2 and 0.6m droplets at the 1k and 2k water molecules scale up to 500 ns. Our simulations show 5k droplets to be the smallest systems whose structural properties are close to those of larger systems, whereas the properties of 1k/2k 0.2m droplets differ noticeably from larger ones and 1k/2k 0.6m droplets are unstable. We will below briefly discuss the data corresponding to those 1k/2k systems.

3 Results and discussion

3.1 NaCl ion pairing in aqueous phase

We discuss here the $[\mathrm{Na}^+, \mathrm{Cl}^-]$ ion pairing in liquid water from the main features of the PMF of a single dissolved $[\mathrm{Na}^+, \mathrm{Cl}^-]$ pair in a periodically replicated box comprising about 1000 water molecules. That PMF has been already intensively investigated in particular by means of quantum Car-Parinello Molecular Dynamics, CPMD, approach,[67] and by means of polarizable force fields based on Drude oscillators and whose parameters were refined to reproduce experimental osmotic pressure data.[30]

As for most ion pairs[68] and as predicted by most of the simulations reported to date for the $[\mathrm{Na}^+, \mathrm{Cl}^-]$ pair (see among others Refs. [69,70]), both the above simulation approaches show that PMF to present a first minimum (termed Contact Ion Pair, CIP) at a short inter ionic distance R_i (about 0.27 nm), then a first maximum (denoted Transition State, TS) at $R_i \approx 0.38$ nm and a second minimum (Solvent Separated Ion Pair, SSIP) at $R_i \approx 0.55$ nm. By setting to zero these PMFs at an inter-ionic distance of 0.6 nm, CPMD predicts the CIP and SSIP energy depths to be about -0.5 ± 0.4 kcal mol^{-1}, whereas the most accurate Drude-based force field predicts these depths to be 0.1 and -0.5 ± 0.1 kcal mol^{-1}, respectively. Lastly, the energy barrier height of TS is about +1.4 kcal mol^{-1} for both approaches. However regarding CPMD results, a recent study shows the overall strong sensitivity of that PMF to the available DFT functionals.[71]

In Figure 2 we plot the $[\text{Na}^+, \text{Cl}^-]$ PMF in liquid water computed from our polarizable force-field approach. Its main features agree with the standard locations of the CIP, TS and SSIP states. Moreover the depths of the CIP and SSIP minima (by shifting to zero the PMF value at $R_i = 0.6$ nm) are in a reasonable agreement with their CPMD and Drude-based counterparts: about -0.9 (CIP) and -0.2 (SSIP) kcal mol^{-1}. The most noticeable difference between our approach and earlier CPMD and Drude-based PMF data concerns the TS energy height: our approach predicts it to be larger by 1.6 kcal mol^{-1} than the later ones. In all our PMF agrees with those computed from CPMD and Drude-based force-field simulations, even we if we may expect our force field to slightly more favor $[\text{Na}^+, \text{Cl}^-]$ ion pairing in liquid water than the latter two approaches (because of the larger energy depth that our force field predicts for CIP).

Our polarizable force field is built to reproduce high level *ab initio* MP2/CBS data regarding small water and ion/water clusters in the gas phase. Hence together with the CPMD scheme[67] and Drude-based force fields[30] refined to reproduce experimental data, all these theoretical methods predict weak energy depths (at the $\text{k}_\text{B}\text{T}$ scale and weaker) regarding the $[\text{Na}^+, \text{Cl}^-]$ CIP and SSIP minima in liquid water.

3.2 Droplet interfaces and ion distributions

The water oxygen and ion mean density functions $\rho(r)$ and $\rho^i(r)$ ($i = \mathrm{Na}^+$, Cl^-) computed at a distance r from the droplet COM are close regardless of the system size and the salt concentration. We plot these functions for 100k droplets in Figure 3 whereas the 5k, 10k, 20k and 1M functions are plotted in Figure S5 of Supporting Information. The water densities $\rho(r)$ exhibit the usual sigmoidal behavior

$$\rho(r) = \frac{\rho_d + \rho_g}{2} + \frac{\rho_d - \rho_g}{2} \left[\tanh\left((r - R_d)/\xi\right)\right]. \tag{6}$$

Here, ρ_d and ρ_g are the mean water densities within the droplet core and the surrounding gas phase. ξ is the thickness of the droplet/gas phase interface, respectively. R_d is the radius of the equimolar dividing surface. To prevent the spurious effects arising from poor statistics at the droplet center, we first adjusted the latter parameters to best reproduce $\rho(r)$ data within -1 to +1 nm from the ideal droplet radius computed from the mean density of neat water at ambient conditions. Then we refine the ρ_d values by averaging $\rho(r)$ within -2 to -1 nm from R_d. The resulting parameters are summarized in Table 1.

Regardless of the droplet size and the salt concentration, the thickness ξ increases from 0.19 (5k) to 0.25 nm (1M) and the radius R_d varies from 3.2 (5k) to 19.2 nm (1M). The radii of 1M droplets are in line with the lower-bound size of the most abundant sub-micron SSAs.[12,14] Below we measure the distances r from the radii R_d. Negative r values indicate the depth into droplet interiors. All the water densities ρ_d at the droplet core are close to the neat water one. They are linearly but weakly correlated to the droplet curvature according to relation (1): the magnitude of the corresponding length δ_ρ is about -0.02 ($0.6m$) and -0.1 ($0.2m$) nm. Curvature effects are thus responsible of stronger pressures within the droplet cores as expected.[44]

The mean ionic densities $\rho^i(r)$ differ at the vicinity of the droplet boundaries for our two kinds of ions (see Fig. 3). Na^+ are repelled from the droplet surface and they tend to slightly accumulate at a distance included between -1.5 and -0.5 nm from R_d. Cl^- are repelled in a lesser extent from the boundaries, however, their density is lower than within droplet cores. The densities of the two ions are half those within the droplet cores at 0.3 (Cl^-) and 0.4 (Na^+) nm before the droplet boundary (regardless of the droplet size and salt concentration) in agreement with earlier experimental-based estimates (that range from 0.31 up to 0.39 nm).[72]

We quantify the difference in the ion behavior at the droplet boundary vicinity from the difference $\Delta\rho^i(r)$ in the Na^+ and Cl^- densities $\rho^i(r)$. From the plots of Figure 3, the functions $\Delta\rho^i(r)$ all present the same profiles: two symmetric peaks at $R_- = -0.3$ nm (peak corresponding to the Cl^- predominance domain) and at $R_+ = -0.9$ nm (Na^+ predominance domain) from R_d. Within the droplet core and starting at R_+, these functions converge then slowly to zero (the convergence is not achieved before $r = -1.9$ nm from R_d). These data show the existence of a weak electric double layer with a separation of about 0.6 nm, and starting at 0.3 nm from the droplet surfaces. Regardless of the salt concentration, the differences among the functions $\rho^i(r)$ for a given ion kind are weak from 10k to 1M droplets. Regarding 5k droplets, their functions $\rho^i(r)$ overall agree with those of larger systems. However in the particular case of the $0.6m$ 5k droplet, we note the function $\rho^{Na}(r)$ to be flatter compared to larger systems within the whole transition layer domain (see Figure S5 of Supporting Information).

$\Delta\rho^i(r)$ functions lead us to define four main domains valid for all our droplets: the droplet core, that extends from the droplet COM up to -1.9 nm from the droplet radius R_d; a transition layer, extending from -1.9 to -0.6 nm from R_d in which Na^+ are slightly dominating; the droplet interface, extending from -0.6 to +0.5 nm from R_d in which Cl^- are dominating in its first half, and above, the gas-phase domain.

The behavior of our ions at the droplet boundary is in line with most of the available data reported from polarizable MD simulations regarding $[\mathrm{Na}^+, \mathrm{Cl}^-]$ aqueous solutions at a larger but still moderate concentration $1m$,[21,25,26] even if overall large differences in the

Cl^- behavior at the close vicinity of the droplet surface exist among these studies. For instance, the $\rho^i(r)$ density for Cl^- can be lower within the full droplet interface domain than within the bulk region[25] like in our simulations, or to be marked by a noticeable peak in that domain, peak whose height is larger than the Cl^- core density.[21,26] We also note a good agreement between our results and earlier non-polarizable simulation data[22,23,29] that were shown to reproduce accurately photoelectron spectroscopy measurements regarding $[Na^+, Cl^-]$ aqueous solutions within the salt concentration range 0.7 - $2.0m$.[23,29] Note also most of the reported experiments, usually performed at higher salt concentrations ($\geq 2m$) to conclude to a weaker repulsion of Cl^- from the droplet boundary than Na^+,[73–75] even if there are controversies regarding the magnitude of that differential behavior.[19]

Lastly, regarding $0.2m$ droplets at the 1k-2k molecular scale, they are stable along multiple independent simulations performed at the 500 ns scale. Their radii R_d are 1.9 and 2.4 nm, respectively, and the ion distributions at the droplet surface vicinity are in line with those of larger systems. However there is a noticeable difference within the droplet core: Na^+ cations are there more abundant than Cl^- anions by 15% (see Figure S6 of Supporting Information). Within those small salty droplets there are thus only two domains, the first close to the interface in which Cl^-dominates and a second interior domain where Na^+dominates. The ion density inhomogeneity within the droplet core is a source of potential instability arising from instantaneous inter ionic repulsive Coulombic effects. To our opinion that explains why 1k-2k $0.6m$ droplets are unstable: they systematically and rapidly split (within 50 ns) in subsystems along all the multiple independent simulations that we performed.

3.3 Ion surface excess

Assuming the gas phase density ρ^i_{g} of a component i to be negligible compared to its droplet core density ρ^i_{d}, the surface excess Γ_{i} of that component can be written as[76]

$$\Gamma_i = \frac{N_i}{4\pi R_e^2} - \frac{R_e \rho^i_{\mathrm{d}}}{3}. \tag{7}$$

Here, N_i is the total number of entities i. We set the radius R_e to zero the water surface excess. From the water ρ_d values summarized in Table 1, we get R_e values that agree with the R_d ones within ± 0.03 nm.

Regarding ions, their droplet core densities ρ_d^i are their mean densities within a spherical shell $\mathbf{S}_d$ extending from R_d-3 to R_d-2 nm (see Table 1). Regardless of the salt concentration, these densities are linearly correlated to the droplet curvature, *i.e.* they obey the standard relation (1) (see Figure S8 of Supporting Information). The length δ_ρ^i is positive and at the 1 nm scale for both our ions. The ρ_d^i densities thus decrease as the droplet size increases. We interpret that behavior as arising from the ion depleted domain at the close vicinity of the droplet boundary and whose extension ($r_{\text{exc}} \approx 0.3$ nm) does not depend on the droplet size. Our ions are thus mainly located within a spherical subdomain of our droplets whose radius is $R_d - r_{\text{exc}}$. That explains the "accessible" volume for our ions (corresponding to the latter spherical subdomains) to be proportionally smaller for small droplets than for larger ones. For instance, the ion "accessible" volume is about 40% smaller than the total droplet volume (as defined from R_d) for 5k droplets, and only 5% smaller for 1M droplets.

In Table 1 we summarized the ion surface excess Γ_i computed from Equation (7) for our droplets. The upper bound of the uncertainties corresponding to the densities ρ_d^i (as computed from a basic block analysis where the domain $\mathbf{S}_d$ is decomposed in ten subdomains of thickness 0.1 nm) amounts to 1%. We use that value together with the mean difference value $R_e - R_d = 0.03$ nm (that we assume to be the uncertainty on the droplet radius R_e) to estimate the uncertainties on Γ_i, which are relatively large, about 20 % of the Γ_i values summarized in Table 1.

For 10 k to 1M droplets, the sum $\Gamma_{\text{tot}} = \Gamma_{\text{Na}^+} + \Gamma_{\text{Cl}^-}$ is a linear increasing function of R_e^{-1}, see Figure 4, and their extrapolated bulk limit values are -0.104 ± 0.020 and -0.228 ± 0.056 nm^{-2} for 0.2 and 0.6m systems, respectively. These bulk values are in a good agreement (within the error bars) with recent experimental-based estimates,[77] see Figure 4, and a priori in a better agreement than values from non-polarizable force fields.[78] Regarding

5k droplets, the $0.2m$ Γ_{tot} value obeys the above linear relation, whereas the $0.6m$ value does not align with larger system data. That suggests a dependence of Γ_{tot} on higher order R_e^{-n} terms for small salty droplets corresponding to molar and larger salt concentrations. However for typical sub-micron SSAs, the standard relation (1) is valid for the quantity Γ_{tot}.

3.4 Salt clusters

At a time t_0, we define a salt cluster as a set of Na^+ and Cl^- ions that are all located at distance shorter than d_{cluster} from at least one another cluster ion. That cluster is considered as surviving until one of its ions leaves it (*i.e.* it is not anymore located at a distance smaller than d_{cluster} from any other cluster ions) or until new ions are added to it.

We set the value of d_{cluster} from the inter-ionic radial distribution functions $g_{\text{ii}}(R_{\text{ii}})$ computed along our simulations. The three kinds of functions, corresponding to $[\text{Na}^+, \text{Cl}^-]$, $[\text{Na}^+, \text{Na}^+]$ and $[\text{Cl}^-, \text{Cl}^-]$ pairs, are shown in Figure 5. These functions agree with those computed from earlier polarizable and non-polarizable MD simulations of aqueous solutions at moderate $[\text{Na}^+, \text{Cl}^-]$ concentrations, see among others Refs. [31,79–81]. In particular, our functions g_{NaCl} all present a first sharp peak located at 0.27 nm and which extends up to 0.32 nm, a distance at which the functions g_{NaNa} and g_{ClCl} start to be non-zero. We thus set d_{cluster} to 0.32 nm. Our cluster definition meets that proposed by Hassan[82,83] and Rick and co-workers[31] to analyze $[\text{Na}^+, \text{Cl}^-]$ aqueous solutions. As the first peak of g_{NaCl} corresponds to $[\text{Na}^+, \text{Cl}^-]$ CIP pairs, this cluster definition allows to identify clusters in which ions are at contact rather than largely incorporating water (with ions in SSIP states, for instance). Note, however, SSIP clusters (and assemblies of clusters) are inferred to represent also a sizable proportion of the ionic assemblies that can be observed in $[\text{Na}^+, \text{Cl}^-]$ aqueous solutions even at low concentrations.[79,84–87]

Regarding 10k-1M systems, our clustering analysis shows a noticeable presence of associated $[\text{Na}^+, \text{Cl}^-]$ pairs within our droplets as well as of larger clusters comprising up to $k = 5$ ions ($0.2m$-10k droplet) and even 10 ones ($0.6m$ droplets). However the probability of observing large clusters is weak as shown by the cluster size distributions computed from our simulations, see Figure 6(a). These functions are computed by considering as a single event a cluster from its apparition to its 'disappearance' according to the above cluster definition rules. These functions are all fast decaying exponential functions of the cluster size and a 10-sized cluster is identified only once along the full 30 ns simulation of the 0.6m-1M droplet. Lastly, 3-sized clusters are relatively abundant as they represent about 10 % of the $[\mathrm{Na}^+, \mathrm{Cl}^-]$ pairs identified.

In Figure 6(b) we plot the percentage n^i_{free} of free Na^+ and Cl^- ions, *i.e.* ions not included in a cluster within the full 10k-1M droplets, as a function of their curvature R_d^{-1}. n^i_{free} increases linearly as R_d^{-1} decreases for both ions, even if that quantity is almost converged for 0.2m droplets as soon as 10k (within the error bars). Regarding 0.6m droplets, $n^i_{\mathrm{free}}(10\mathrm{k})$ data are still far from being converged compared to 1M ones. Another striking difference between 0.2m and 0.6m droplets is the dissymmetric behavior between Na^+ and Cl^-: in 0.6m droplets, the amount of free Na^+ is larger than free Cl^-, by 4 (10k) to 7 (1M) %. Such a dissymmetry also exists for 0.2m droplets but the difference in free Na^+ and Cl^- is less accented (about 1%). To our opinion the dependence of the n^i_{free} quantities to the droplet radius R_d may be interpreted as for the ion densities ρ^i_d within the droplet bulk-like core domains, *i.e.* that dependence arises from the ion exclusion shell at the close vicinity of the droplet boundary, whose extension does not depend on the droplet size.

However the percentages of free ions within the droplet interface domains (where Cl^- ions dominate) are far to meet the percentages computed within the full droplet. In Table 2, we summarized the mean quantities n^i_{free} corresponding to the droplet bulk-like core, transition layer and interface domains. These data show free Na^+ to dominate over free Cl^- within the droplet core, contrary to what is observed at the vicinity of the droplet boundary where free Cl^- are more abundant than Na^+ by about 5%, regardless of the salt concentration and the droplet size.

In Figure 6(d) we plot the mean number of Na^+ per cluster as a function of the cluster size for $0.6m$ droplets. The compositions of clusters comprising more than 2 ions are dissymmetric: they contain noticeably more Cl^- than Na^+ even for even-sized clusters. That is also observed for $0.2m$ droplets. However the relative abundance of Na^+ *wrt* the cluster size obeys two linear regimes: for large clusters (whose size k is ≥ 5), the proportion of Na^+ is reinforced compared to smaller clusters, even if large clusters still comprise more Cl^-. The weaker proportion of Na^+ within clusters may be interpreted as arising from the slightly larger stability of the symmetric linear trimer $[NaCl_2{}^-]$ compared to $[Na_2Cl^+]$, by about 3 kcal mol^{-1} in the gas phase, as predicted by quantum MP2/CBS computations and our force field, see Figure S3 of Supporting Information. The polarizability of Na^+ is one order of magnitude smaller than the Cl^- one. The electric fields arising from the two lateral ions on the central ones in both the linear trimers cancel out and that explains the relative stability of the latter trimers.

Up to relatively large sizes (k=7-8), the clusters are usually planar on average. For $k \geq 5$ the structure of the most abundant clusters correspond to a $[Na^+, Cl^-]$ symmetric hetero tetramer to which a few more ions (preferentially Cl^-) are connected. Three-dimensional structures are observed only in 9- and 10-sized clusters: one or two Cl^- are then connected to an almost cubic and symmetric salt octamer, see the cluster snapshots shown in Figure 7, for instance.

Our $0.6m$ fractions of free ions extrapolated to the bulk limit (*i.e.* $R_d^{-1} \to 0$) meet those reported from polarizable MD simulations of $[Na^+, Cl^-]$ $1m$ aqueous solutions performed by Rick and co-workers.[31] The force-field parameters in the latter study were refined to reproduce osmotic pressure experimental data. However contrary to our results, there is an excess of Na^+ within the salt clusters identified along the $1m$ simulations of Rick and co-workers and that yields thus a slight predominance of Cl^- among the free ions in the latter simulations. The parameters of our force field are assigned from a different *ab-initio*-based strategy. However both our data and the latter one clearly support noticeable association phenomena of Na^+ and Cl^- ions in aqueous solutions from low to moderate concentrations

$\leq 1m$, as also predicted by non-polarizable simulations, see below. However we may note the opposite conclusion drawn from MD simulations performed by means of the sophisticated reactive force field ReaxFF[81] and which predict $[\mathrm{Na}^+, \mathrm{Cl}^-]$ to be already fully dissociated at the $1m$ concentration.

We estimated the mean survival time t_s^k of k-sized clusters from the probability survival function $p_i^k(t_0, t_0 + n\tau^*)$ of a given cluster i of size k identified along a simulation. τ^* is the time sampling interval of our MD trajectories (set to 10 ps) and the survival function of a particular cluster is equal to one at all the times $t_0 + l\tau^*$ $(0 \leq l \leq n)$ if that cluster is observed at all the n successive sampled simulation snapshots starting at t_0, and zero otherwise. From the survival functions of all the M_k clusters of size k identified along a simulation, we compute the mean correlation function

$$C_k(l\tau^*) = \left\langle \frac{1}{M_k} \sum_{i=1}^{M_k} p_i^k(t_0, t_0 + l\tau^*)) \right\rangle_{t_0} . \tag{8}$$

We show these correlation functions to obey (see Figure S10 of Supporting Information):

$$C_k(t) = \exp(-t/t_s^k). \tag{9}$$

Here, t_s^k is the mean cluster survival time and its values for the most abundant clusters are reported in Table 3. They range from 130 to 470 ± 15 ps and the larger ones correspond mainly to the larger clusters, regardless of the salt concentration and the droplet size. The order of magnitude of our values t_s^k (and their closeness) matches that computed by Hassan from non-polarizable MD simulations of $[\mathrm{Na}^+, \mathrm{Cl}^-]$ aqueous solutions (whose concentration ranges from 0.1 to $3m$).[82] Interestingly, both the Hassan's and our t_s^k estimates also match that computed for large clusters $(k \geq 6)$ in supersaturated $[\mathrm{Na}^+, \mathrm{Cl}^-]$ aqueous solutions $(c \geq 14m)$ from non-polarizable MD simulations.[88]

Regarding the most abundant 2 and 3-sized clusters identified along our simulations, we plot in Figure 8 their normalized radial distribution $g_{\mathrm{cluster}}^{k=2,3}(r)$ as a function of the distance

r of the cluster COM from the droplet boundary for 100k systems. The functions for 10k and 1M systems are fully in line with the latter ones. For $0.6m$ droplets, both $[\mathrm{Na}^+, \mathrm{Cl}^-]$ pairs and 3-sized clusters are repelled from the droplet surface as individual Na^+, and that behavior is more accented for $0.2m$ droplets. Salt clusters are thus mainly observed within droplet bulk-like core domains. We also note a large diffusion of salt clusters across the droplet core, transition layer and interface domains: up to 90% of the salt clusters originally formed within the transition layer and interface domains vanish or incorporate new ions in a different droplet domain.

Regarding the smallest 5k droplets, most of the results discussed above for larger systems are still valid. However we note much weaker percentages of free ions in 5k droplets, percentages that drop to 80 % ($0.2m$) and even 55-60 % ($0.6m$), regardless of the droplet domain and ion type, see Table 2. We note even a stronger probability to observe large clusters (up to 10 sized ones) within the 5k $0.6m$ droplet than within larger systems, see Figure 6(a). To our opinion that arises from the proportionally weaker ion 'accessible' volume in 5k droplets compared to larger systems (see above), which favors ion clustering. Accounting also for the ion surface excess data regarding the $0.6m$ 5k droplet, the ion behavior within droplets appears to obey two regimes, the first, that we term as 'curvature linear' regime, for droplets whose molecular size is as small as 10k and a more complex regime for smaller droplets.

3.5 Surface potential

As our systems are all quasi spherical, we solve the Poisson's equation to estimate the electrostatic potential Φ at a distance r from the droplet COM according to

$$\Phi(r) = -\frac{1}{\epsilon_0} \int_0^r \frac{C_q(r) + C_p(r)}{r^2} dr. \tag{10}$$

$C_q(r)$ is the mean sum of the static charges included in a sphere of radius r and $C_p(r)$ is the mean density at distance r of the induced dipole projections in the radial direction.

We discretely computed these functions from our simulation data with dr set to 0.01 nm. The $\Phi(r)$ plots for 100k droplets are shown in Figure 9(a). The surface potential $\Delta\Phi$ of our systems is the difference in the $\Phi(r)$ values corresponding to $r = R_d - 2$ and $R_d + 1$ nm.

For 10k-1M salty droplets and as already reported for pure water systems,[51] the surface potentials $\Delta\Phi$ of all our systems are linearly correlated to the droplet curvature R_d^{-1}, see Figure 9(b). The extrapolated planar interface values $\Delta\Phi(\infty)$ are almost equal : -221 (0.2m) and -217 (0.6m) ± 3 mV. They are close to our $\Delta\Phi$ estimate for neat water as using our water model TCPE/2013: -227 mV.[51] Note the δ_Φ length is larger for 0.6m droplets than for the 0.2m ones, 0.32 and 0.51 ± 0.07 nm, respectively (for neat water $\delta_\Phi = 0.14$ nm[51]).

According to Equation (10) the surface potentials $\Delta\Phi$ are the sum of the static charge and induced dipole components $\Delta\Phi_q$ and $\Delta\Phi_p$. For pure water systems, the latter components are negative and their ratio is about 3:1.[51] For our NaCl droplets, the $\Delta\Phi$ values are dominated by the induced dipole components $\Delta\Phi_p$, regardless of the salt concentration.

Regarding neat water and 1.1-2.1m NaCl aqueous solutions, Ishyama and Morita[21] also decomposed the surface potentials in their $\Delta\Phi_q$ and $\Delta\Phi_p$ components from MD data generated using an induced dipole-based polarizable force field whose parameters were assigned to reproduce experimental data regarding neat water and electrolyte aqueous solutions at ambient conditions. Contrary to our results, the latter authors showed the ratio of the $\Delta\Phi_q$ and $\Delta\Phi_p$ components of their salty solutions to be about 3:1, *i.e.* the $\Delta\Phi_q$ contributions are thus dominating. However in line with our 0.6m data, the latter authors concluded the surface potential $\Delta\Phi$ of neat water and of their salty solutions to be equal (within 6 mV), even if their $\Delta\Phi$ values are about twice as large as our own.

Taking in mind the overall large variability of the theoretical values $\Delta\Phi$ reported for neat water from both polarizable and non-polarizable force fields (see among others the values reported in Ref. 89), to our opinion the differences between our $\Delta\Phi$ values and those reported by Ishyama and Morita arise from the different strategies used to adjust the force-field parameters. However both our force field and that of the latter authors predict the same trends for the change in the $\Delta\Phi$ values from neat water to low/moderately concentrated salty NaCl aqueous solutions, *i.e.* the presence of salt has a weak effect on the surface potential of aqueous solutions. Experimentally, Jarvis and Scheiman[90] reported differences in $\Delta\Phi$ values between NaCl aqueous solutions (whose concentrations c are $< 1m$) and neat water to be about +1 mV whereas a recent experimental study of Allen and co-workers showed that difference to be +120 mV for $c = 1m$.[91] Both our estimates of $\Delta\Phi$ and the earlier ones of Ishyama and Morita support thus the earlier experimental estimate of Jarvis and Scheiman.

Regarding 5k droplets and regardless of c, their $\Delta\Phi$ values differ noticeably from the expected values extrapolated from the data of larger systems, see Figure 9(b). Accounting also for the structural and ion clustering data discussed above, the properties of salty 0.2 and $0.6m$ droplets thus obey a linear regime of the droplet curvature down to a molecular size included between 5k and 10k. That corresponds to a droplet radius of about 3 nm.

3.6 Water vapor density and the Kelvin term

The Kelvin term is one of the main components of the Köhler's equation[39] commonly used to discuss the stability of SSAs in the atmosphere and the formation of cloud condensation nuclei (see among others Ref. 16). The historical (standard) Kelvin term relates the equilibrium vapor pressure p_d to the radius R_d of a spherical liquid droplet according to

$$p_d = p_\infty \exp\left(\frac{2\gamma_\infty}{\mathrm{RT}\rho_\infty R_d}\right). \tag{11}$$

Here, p_∞ and γ_∞ are the saturation pressure and the surface tension of the liquid (planar interface)/gas phase equilibrium, respectively. ρ_∞ is the density of the liquid phase, and R is the ideal gas constant. Assuming the water vapor at ambient conditions to be an ideal gas, we may rewrite the Kelvin term in a logarithmic form as

$$\ln \rho_d^g = \ln \rho_\infty^g + \frac{2\gamma_\infty}{\mathrm{RT}\rho_\infty} \times \frac{1}{R_d}, \tag{12}$$

here, ρ_d^g and ρ_∞^g are the water vapor densities corresponding to the droplet/vapor and liquid water/vapor equilibrium, respectively. Simulations based on our force field predict γ_∞ to amount to 63.3, 64.3 and 64.4 ± 0.1 mN m^{-1} for neat water, $0.2m$ and $0.6m$ NaCl solutions at ambient conditions, respectively (see Supporting Information). These values are about 10 % smaller than experiment, but they lie within the range of values reported from earlier simulations based on different force fields.[26] However, and at the difference of many of these earlier simulations, our data predict weak positive increments of the surface tension from neat water to salty solutions (at weak and moderate concentrations) in agreement with experiment.[92]

Because of the sub-micron scale of our droplets, it is more reasonable to consider a modified version of the standard Kelvin term based on the droplet surface tension γ_d that obeys the Tolman relation[93]

$$\gamma_d = \gamma_\infty \left(\frac{R_d}{R_d + 2\delta_\gamma} \right). \tag{13}$$

Here δ_γ is the Tolman length. Neglecting the weak curvature dependence of the water density within the droplets core (see above), that yields the water vapor densities to obey

$$\ln \rho_d^g = \ln \rho_\infty^g + \frac{2\gamma_\infty}{\mathrm{RT}\rho_\infty} \times \frac{1}{(R_d + 2\delta_\gamma)}. \tag{14}$$

As the cavities in which our droplets lie are large enough, we computed from our simulations the water mean molecular densities ρ_d^g of the vapor phase surrounding the droplets within a spherical shell extending from +1 to + 2 nm from the droplet surfaces. Water radial distribution functions $\rho(r)$ within those shells are plotted in Figure S14 of Supporting Information as a function of the distance r from the surface for 10k to 1M salty droplets. Those plots show converged ρ_d^g densities that decrease from about 1.0 down to about 0.5 10^{-3} molecule nm^{-3} as the droplet size increases. Those density values agree with the vapor density corresponding to liquid water, about 0.8 10^{-3} molecule nm^{-3} from experimental data at ambient conditions. We computed the uncertainty of our mean vapor density from a standard block analysis method (see Figures S12 and S13 of Supporting Information). For droplets simulated at the 100 ns scale and above (5k to 100k), that uncertainty is about 8%, whereas it amounts to about 16% for the 1M droplets that were simulated at the 30 ns scale. Note also that we performed multiple simulations of 1k pure aqueous droplets at the 500 ns scale: the water vapor densities computed along all these simulations agree within the error bars computed from the standard block analysis method.

The plots of the quantities $\ln(\rho_d^g)$ as a function of the droplet curvature R_d^{-1} reported in Figure 10 show the water vapor densities ρ_d^g to obey (within the error bars) a Kelvin term based on droplet surface tensions γ_d corresponding to a negative Tolman length at the 1 nm scale, *i.e.* δ_γ = -0.85 ± 0.05 nm, regardless of the salt concentration. We also investigated pure water droplets whose molecular size ranges from 1k to 20k according to our modeling protocol. The simulations were performed at the 500 ns (1k-2k), 200 ns (5k-10k) and 100 ns (20k) scale. In agreement with all the theoretical data reported to date,[42–44] our simulations suggest for pure water droplets a weak and a priori negative Tolman length δ_γ (at least -0.1 nm, see Figure S11 of Supporting Information).

The vapor densities ρ_∞^g corresponding to neat water and salty aqueous planar interfaces that allow us to best reproduce our ρ_d^g data amount to about 0.52 (salty solutions) and 0.64 (neat water) 10^{-3} molecule nm^{-3}. Our simulations predict thus large NaCl SSAs to be stable in the atmosphere at a relative humidity of about 80 %, in agreement with experiment.[14] Along our simulations of planar interfaces, we also computed the corresponding water vapor densities ρ_∞^g. Their order of magnitude agrees with the above extrapolated estimates. However these data suffer from large uncertainties (about 30-40% of the ρ_∞^g values, see Figure S14 of Supporting Information). To our opinion that arises from the weak extension of the surfaces (and from the overall large volume of the vapor phase) of the simulated planar interfaces. Compared to them, the boundary surfaces of 5k to 1M droplets (and thus the number of water molecules able to escape from the droplet surface) are from 16 up to 500 times larger.

4 Conclusion

We have investigated at ambient temperature $[\mathrm{Na}^+, \mathrm{Cl}^-]$ salty aqueous droplets whose water molecular sizes vary from 1k to 1M and whose salt concentrations are $0.2m$ (brackish water) and $0.6m$ (sea water) using a polarizable *ab initio*-based force field and MD simulations at the 500 (1k/2k), 200 (5k/10k), 100 (100k) and 30 (1M) ns scale. Because of their size and composition, 100k and 1M salty droplets correspond to ideal sub-micron SSAs as being produced by oceans.

Regarding large systems (from 5k to 1M), our simulations show $[\mathrm{Na}^+, \mathrm{Cl}^-]$ droplets to be organized in three main domains: the interface domain (at the vicinity of the droplet boundary and where Cl^- dominate within the droplet interior sub-region), then the transition layer (where Na^+ dominate at its upper boundary) and finally the bulk-like core domain corresponding to a homogeneous salty solution. Interestingly, the spatial extension of these domains does not depend on the droplet size and composition. By measuring the distances from the droplet boundary, the interface domain extends from +0.5 to -0.6 nm (with a maximum of the Cl^- over concentration relative to Na^+ at -0.3 nm), the transition layer extends from -0.6 down to -1.9 nm (with a maximum of the Na^+ over concentration relative to Cl^- at -0.9 nm), and the bulk-like core domain starts at -1.9 nm. Compared to earlier simulations the most striking discrepancies concern the composition of large $[\mathrm{Na}^+, \mathrm{Cl}^-]$ aggregates that may be observed in aqueous environments: our droplet simulations show Cl^- to dominate in all the most probable aggregates larger than dimers whereas earlier bulk simulations also based on a polarizable force field but adjusted from experimental data predict the contrary. As the parameters of our force field are assigned only from quantum data that show the isolated linear trimer $[(\mathrm{Cl}^-)_2, \mathrm{Na}^+]$ to be more stable than $[(\mathrm{Na}^+)_2, \mathrm{Cl}^-]$, that clearly suggests the need of accounting for quantum data regarding small molecular aggregates while building a force field to reproduce macroscopic experimental properties.

Contrary to ion spatial distributions, the magnitude of the properties A that we investigated (like surface potential, ion surface excess and ion droplet-core densities) for large droplets are linearly correlated to the droplet curvature R^{-1} according to

$$A = A_\infty \left(1 - \frac{2\delta_A}{R}\right) + O(\frac{1}{R^2}). \tag{15}$$

Here A_∞ is the extrapolated bulk (planar interface) value of the quantity A and δ_A is a length whose sign and magnitude measure the surface curvature effect on A. Regarding the reliability of our simulations, we note all the extrapolated data A_∞ estimates to be in line with or included within most of the available experimental and theoretical data. Regarding the magnitudes of the lengths δ_A they amount from a few tenths of nm up to at most a few nm. Interestingly, our simulations show the surface tension of NaCl salty droplets to obey the Tolman relation with a Tolman length negative and at the 1 nm scale, whereas our simulations of 1k to 20k pure aqueous droplets yield a much weaker Tolman length (about -0.1 nm) for neat water droplets in agreement with earlier studies based on different molecular modeling approaches.[42–44] Lastly the limit of validity of the above relation corresponds to droplets whose size is included between 5k and 10k, *i.e.* droplets whose radius is about 3-4 nm.

Another important difference between pure aqueous and salty droplets is the stability of small droplets whose molecular size is lower than 5k. Our simulations show salty systems to present a source of instability arising from the lack of a homogenous ionic domain at their center contrary to larger systems. To our opinion that explains the splitting of 1k and 2k 0.6m droplets in smaller subsystems at the early stages of multiple independent simulations, whereas 1k/2k pure water droplets are stable along multiple 500 ns scale simulations (*i.e.* they correspond to quasi-spherical liquid nanodrops whose radius is constant along the simulations, on average).

The uncertainties regarding our data prevent us to further investigate the dependence of droplet properties to higher order curvature terms R^{-n} ($n > 1$). In all our data regarding 10k to 1M salty droplets show their properties to be usually well reproduced using a standard and simple linear relation of the droplet curvature. Regarding the surface tensions of our salty droplets, they a priori obey the Tolman relation. However as the magnitude of the Tolman length δ_γ is about 1 nm and because of the uncertainties regarding water vapor densities, our surface tension data may also obey to more complex laws as those discussed in Refs.[94,95].

Our 10k to 1M salty droplets corresponds to ideal sub-micron SSAs that might dominate the aerosol distributions at marine boundary layers.[17,18] Regarding atmospheric science, our surface tension results support the validity of the Kelvin relation in its droplet form, see Eq. (11), to model salty SSAs whose radius is as small as 3-4 nm. Together with the water activity a_w, the Kelvin term is the second component of the Köhler equation relating the ambient relative humidity RH to the SSA radius R_d according to

$$\mathrm{RH} = a_w \times \exp\left(\frac{2\gamma_d}{\mathrm{RT}\rho_l R_d}\right). \tag{16}$$

Assuming a standard relation for the water activity a_w,[16] the effect of a negative Tolman length at the 1 nm scale yields to weaken the number of sub-micron NaCl SSAs that might activate for RH values included between 1.003 and 1.01 (and thus evolve towards stratocumulus and warm cumulus clouds as usually inferred[16]) by a few percents as compared to the prediction of a standard Köhler equation based on infinite planar surface tension data (see Figure S15 of Supporting Information). However marine sub-micron scale SSAs are enriched by organic materials that may alter their properties as compared to the ideal salty droplets that we studied here. We are presently simulating salty aqueous SSAs in presence of fatty acids by means of new polarizable force fields[96] to further assess the behavior of more complex sub-micron SSAs.

Supporting Information

All the plots mentioned as supplementary materials in the manuscript are provided as Supporting Information. Details regarding the computations of surface tensions from planar interface simulations, the short range many body functions to improve the modeling of ions in aqueous environments as well as the computations of cumulative condensation nuclei from the Kölher relation are also provided as Supporting Information. Lastly, the raw data computed along our simulations of the ion and salt clusters (from dimers to pentamers) radial distribution functions, as well as of the functions $C_q(r)$ and $C_p(r)$ to compute the surface potentials are also provided as Supporting Information.

Acknowledgments

This work was granted access to the TGCC HPC resources under the Grand Challenge allocation [GC0429] made by GENCI. We acknowledge support by the French government through the Program "Investissement d'avenir" (LABEX CaPPA / ANR-11-LABX-0005-01 and I-SITE ULNE / ANR-16-IDEX-0004 ULNE), as well as by the Ministry of Higher Education and Research, Hauts de France council and European Regional Development Fund (ERDF) through the Contrat de Projets État-Région (CPER CLIMIBIO). We further acknowledge the "Groupement de recherche" GDR 2035 SolvATE.

Table 1: Main droplet properties. N_{pair}: number of ion pairs in 0.2 and 0.6m systems. R_d and η_d: mean droplet radius and thickness (in nm). $\Gamma_{\mathrm{Na^+/Cl^-}}$: ion surface excess in nm^{-2}. ρ_d and $\rho_d^{(\mathrm{Na^+,Cl^-})}$: mean water and ion densities within the droplet bulk-like core domain (expressed in molecules(ions) nm^{-3}).

Droplets	c	N_{pair}	R_d	η_d	ρ_d	$\Gamma_{\mathrm{Na^+}}$	$\Gamma_{\mathrm{Cl^-}}$	$\rho_d^{\mathrm{Na^+}}$	$\rho_d^{\mathrm{Cl^-}}$
5k	0.2m	15	3.2	0.195	33.75	-0.0691	-0.0629	0.0161	0.0167
	0.6m	49	3.2	0.192	33.29	-0.2218	-0.2180	0.0542	0.0539
10k	0.2m	37	4.0	0.205	33.63	-0.0691	-0.0668	0.0185	0.0184
	0.6m	102	4.0	0.205	33.29	-0.1204	-0.1276	0.0486	0.0491
20k	0.2m	53	5.0	0.215	33.63	-0.0526	-0.0502	0.0129	0.0122
	0.6m	176	5.0	0.212	33.27	-0.1361	-0.1313	0.0436	0.0448
100k	0.2m	398	8.9	0.243	33.39	-0.0572	-0.0576	0.0152	0.0152
	0.6m	1038	9.0	0.239	33.17	-0.1214	-0.1245	0.0380	0.0381
1M	0.2m	4000	19.2	0.254	33.33	-0.0561	-0.0566	0.0141	0.0143
	0.6m	10000	19.2	0.253	33.12	-0.1136	-0.1137	0.0356	0.0357

Table 2: Percentages of free ions in the three main droplet domains, in %. Their mean uncertainty is ± 2 %.

Size	bulk-like core		transition layer		interface	
	Na^+	Cl^-	Na^+	Cl^-	Na^+	Cl^-
$0.2m$						
5k	80.6	77.8	83.0	76.8	74.2	86.5
10k	90.0	89.0	90.6	87.6	88.2	93.0
20k	92.8	91.7	92.8	90.9	91.0	95.4
100k	91.3	90.6	91.8	90.0	89.8	94.6
1M	91.3	90.8	92.0	90.6	90.7	94.7
$0.6m$						
5k	60.1	46.0	65.2	47.6	63.9	53.0
10k	76.9	69.6	79.8	70.0	78.3	82.9
20k	79.9	75.1	81.4	72.9	79.9	84.4
100k	81.8	77.5	83.8	77.7	82.9	86.6
1M	82.6	79.2	84.1	79.4	82.5	88.2

Table 3: Mean survival times t_s^k of the most abundant salt clusters of size $k = 2, 3$ and 4. All values in ps. Their mean uncertainty is ± 15 ps.

Cluster size	2	3	4
$0.2m$			
5k	148	158	120
10k	140	215	104
20k	135	215	470
100k	130	197	330
1M	137	190	249
$0.6m$			
5k	144	172	213
10k	133	175	291
20k	126	176	352
100k	130	187	326
1M	136	202	359

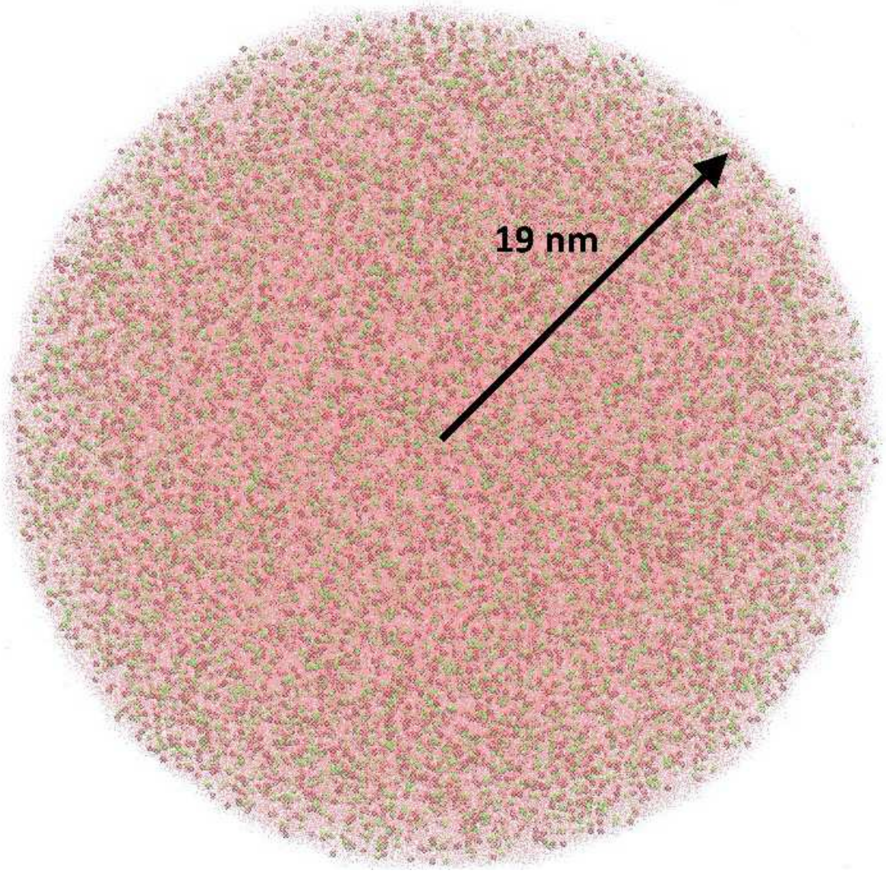

Figure 1: Relaxed structure of the 1M droplet corresponding to a salt concentration of 0.6m (and comprising 10 000 $[\mathrm{Na}^+, \mathrm{Cl}^-]$ pairs). Water molecules are shown in red in a transparency mode, whereas green and red spheres correspond to ions.

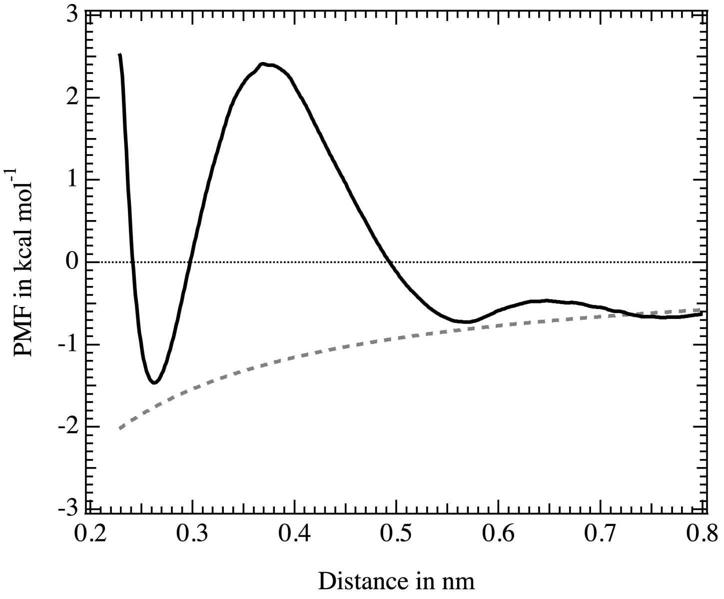

Figure 2: $[\mathrm{Na}^+, \mathrm{Cl}^-]$ ion pair PMFs in neat liquid water at ambient conditions as computed from our force fields (black line). Dashed grey line, the expected Coulombic PMF corresponding to two point charges of opposite sign in bulk water at ambient conditions. Our simulated PMF is shifted to meet the Coulombic PMF value at 0.8 nm.

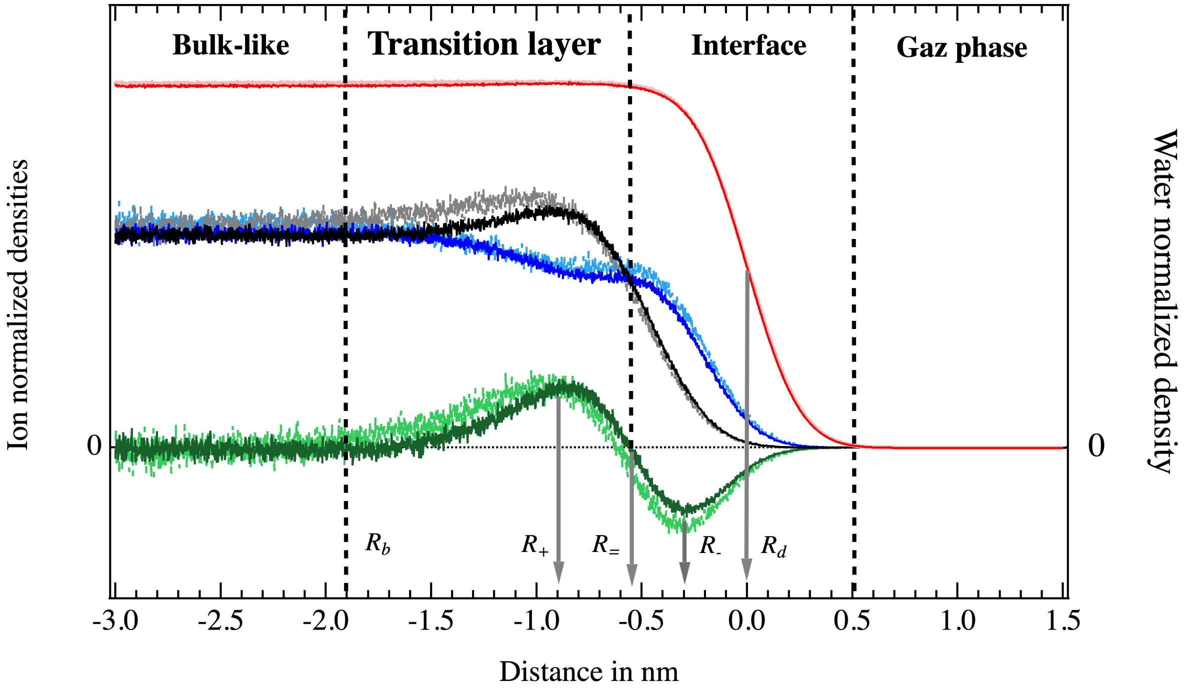

Figure 3: Ion (left axis) and water (right axis) normalized densities as a function of the distance from the mean droplet radius R_d for 100k droplets. Negative distances correspond to the droplet interior. Water, Na^+ and Cl^- densities are plotted in red, black and blue lines, respectively. $0.2m$ data are plotted in lighter colors than $0.6m$ ones. Green lines: differences $\Delta\rho^i(r)$ in the Na^+ and Cl^- densities. The vertical grey arrows are located at the minimum, zero and maximum values of the $\Delta\rho^i(r)$ functions and at the mean droplet radius. The vertical black dashed lines delimit the four main domains from the droplet core to the gas phase. The profiles for 5k and 1M droplets are fully in line with the present 100k ones (see Supporting Material).

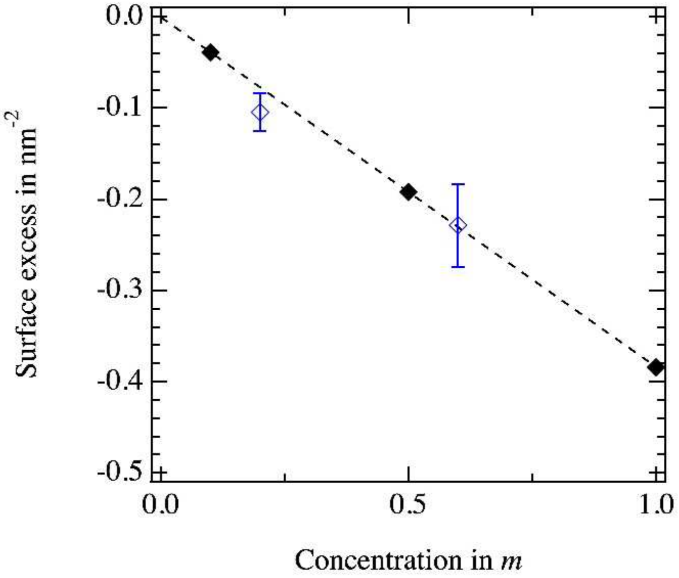

Figure 4: Up: total ion surface excess values Γ_{tot} as a function of the salt concentration. Blue and black: 0.2 and 0.6m data, respectively; dashed lines: the corresponding linear regression fits. Down: converged bulk values for Γ_{tot} (blue symbols) compared to the experimental-based estimates[77] (black symbols, the dashed lines correspond to the linear regression fit of the experimental values).

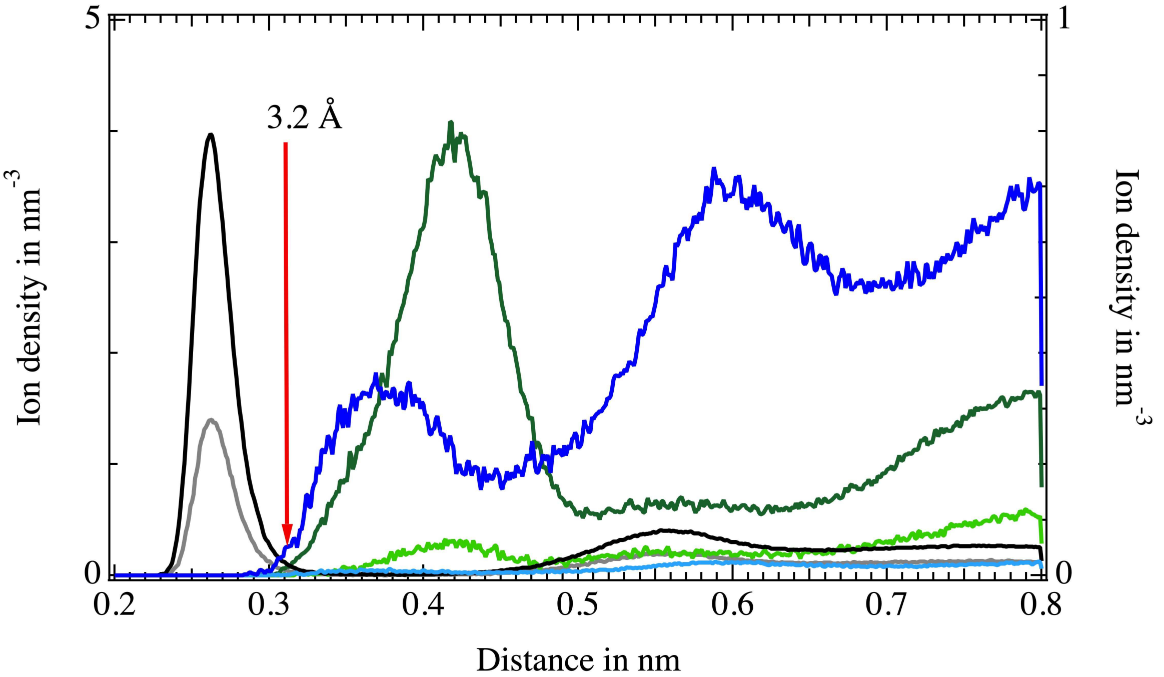

Figure 5: Ion pair radial distribution functions $g_{\mathrm{ii}}(r)$ within the 100k droplet bulk-like core domains. Black and grey lines: $[\mathrm{Na}^+, \mathrm{Cl}^-]$ pairs; blue and light blue lines: $[\mathrm{Na}^+, \mathrm{Na}^+]$ pairs; green and light green lines: $[\mathrm{Cl}^-, \mathrm{Cl}^-]$ pairs. $0.2m$ data (right axis) are shown in lighter colors than $0.6m$ data (left axis).

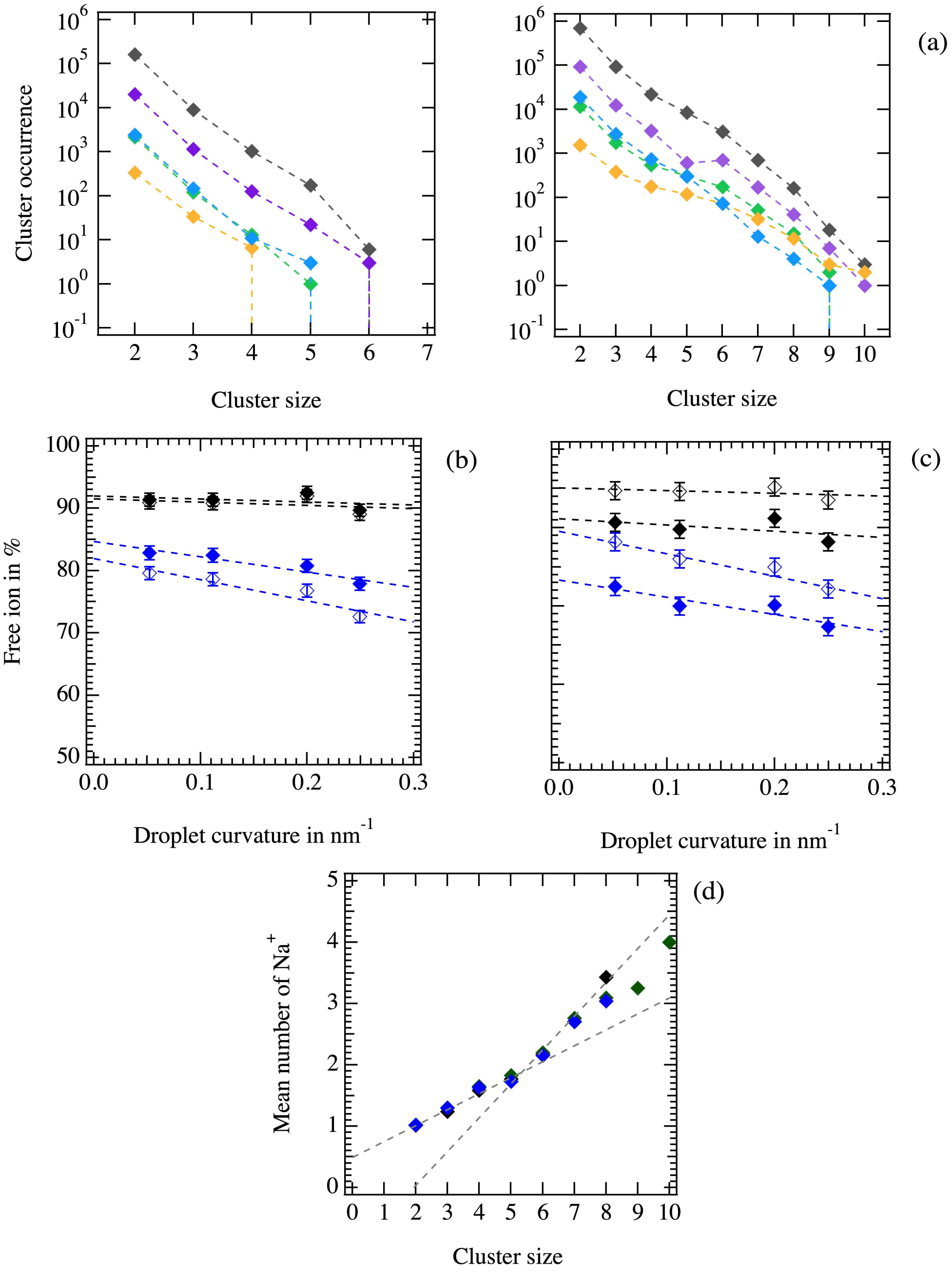

Figure 6: (a) Salt cluster distributions as a function of their size for 0.2m (left) and 0.6m (right) droplets. Grey, violet, blue, green and orange: data for 1M, 100k, 20k, 10k and 5k droplets. (b) Percentages of free ions within the full droplets as a function of R_d^{-1}. (c) Percentages of free ions within the droplet interface domains as a function of R_d^{-1}. For (b) and (c), full and empty symbols: Na^+ and Cl^- data; black and blue symbols: 0.2m and 0.6m droplet data (here we consider the data of only 10k to 1M droplets). Dashed lines: linear regression fits (the regression coefficients are all > 0.95). (d) Mean number of Na^+ in salt clusters as a function of their ionic size in 0.6m droplets. Black, blue and green: 10k, 100k and 1M data.

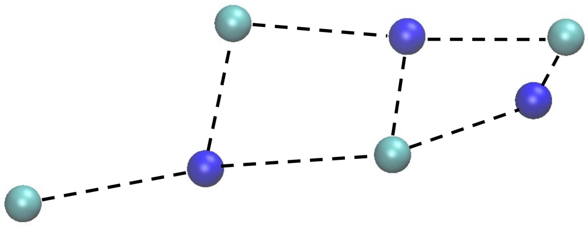

An example of 7-sized salt clusters

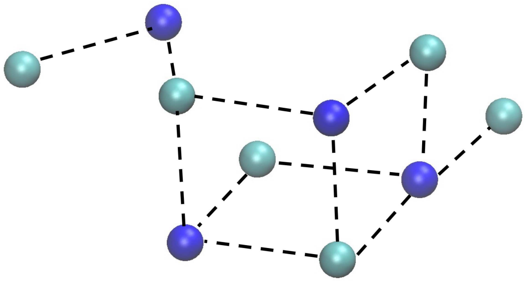

An example of 10-sized salt clusters

Figure 7: Examples of 7 and 10-sized salt clusters identified along our MD simulation of the $0.6m$ 1M droplet. Na^+ and Cl^- are shown in dark and light blue, respectively. Dashed lines connect ions interacting at short range, from 0.254 and 0.282 nm.

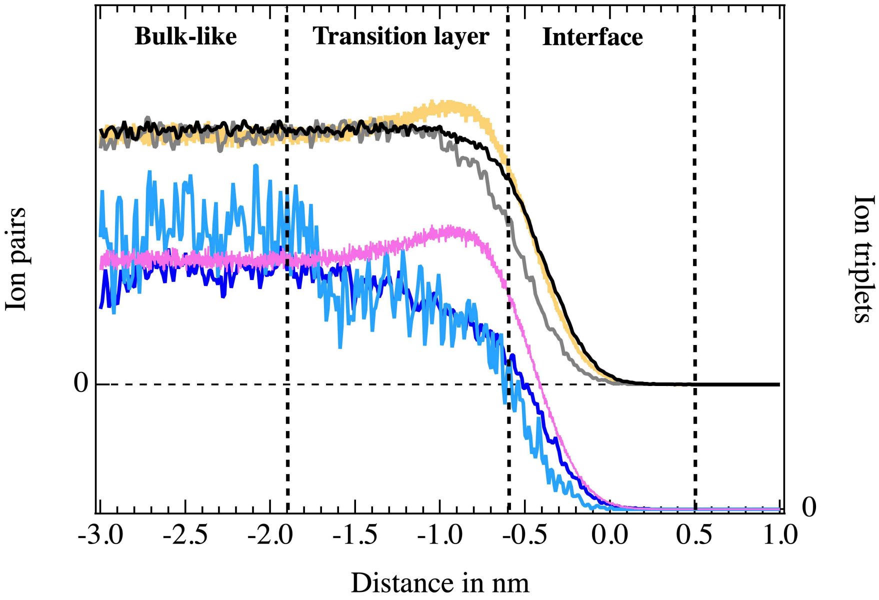

Figure 8: Normalized radial distribution functions of the salt pairs (black and grey lines, left axis) and trimers (blue and light blue lines, right axis) for 100k droplets (light colors correspond to $c = 0.2m$). In light orange and violet lines: the radial distribution of Na^+ for the $0.6m$ 100k droplet for comparison purposes. Note the zero of the left and right axes are shifted for readability purposes.

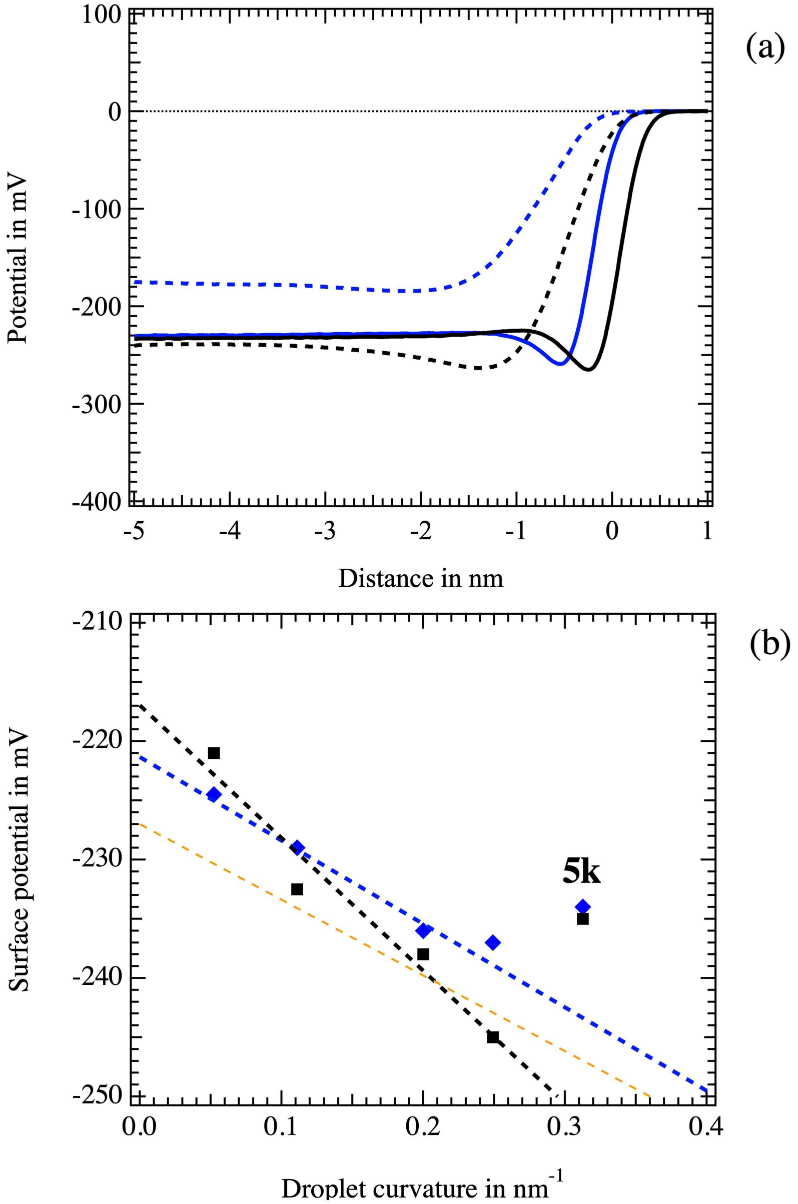

Figure 9: (a) Surface potentials $\Phi(r)$ as a function of the distance r from the droplet boundary for 100k systems. Black and blue: 0.6 and 0.2m data, respectively. Full and dashed lines: full surface potentials and their induced dipole components. (b) Surface potential $\Delta\Phi$ as a function of the droplet curvature R_d^{-1} (in nm^{-1}). Black and blue: 0.6 and 0.2m data. Dashed lines: linear regression fits from data corresponding to droplets larger than 5k (in orange our former result for neat water[51]).

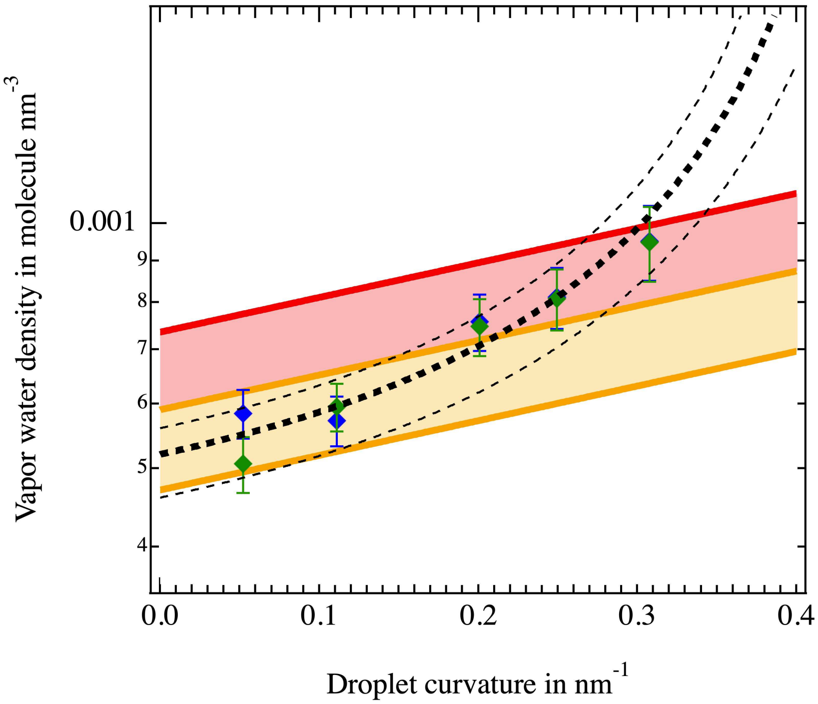

Figure 10: Water vapor density (ln scale) as a function of the droplet curvature R_d^{-1}. Green and blue diamonds: 0.2 and 0.6m data. Bold dashed line: best interpolation of the raw data according to relation (11) and using a Tolman length δ_γ set to -0.85 nm. Thin dashed lines: best interpolations of the data accounting for the uncertainties (upper line, δ_γ = -0.9 nm, lower line: δ_γ = -0.8 nm). Red and orange bold lines: standard Kelvin terms ($\delta_\gamma = 0$) to reproduce 5k (red), 20k (upper orange) and 100k (lower orange) data.

References

(1) Finlayson-Pitts, B. J.; Ezell, M. J.; Pitts, J. N. Formation of Chemically Active Chlorine Compounds by Reactions of Atmospheric NaCl Particles with Gaseous N_2O_5 and $ClONO_2$. *Nature* **1989**, *337*, 241–244, DOI: `10.1038/337241a0`.

(2) Saykally, R. Air/Water Interface: Two Sides of the Acid-Base Story. *Nature Chem.* **2013**, *5*, 82–84, DOI: `10.1038/nchem.1556`.

(3) Ruiz-Lopez, M. F.; Francisco, J. S.; Martins-Costa, M. T. C.; Anglada, J. M. Molecular Reactions at Aqueous Interfaces. *Nat. Rev. Chem.* **2020**, *4*, 459–475, DOI: `10.1038/s41570-020-0203-2`.

(4) Reis, P.; Holmberg, K.; Watzke, H.; Leser, M.; Miller, R. Lipases at Interfaces: A Review. *Adv. Colloid Interfac.* **2009**, *147-148*, 237–250, DOI: `10.1016/j.cis.2008.06.001`.

(5) Serrano-Luginbühl, S.; Ruiz-Mirazo, K.; Ostaszewski, R.; Gallou, F.; Walde, P. Soft and Dispersed Interface-Rich Aqueous Systems that Promote and Guide Chemical Reactions. *Nat. Rev. Chem.* **2018**, *2*, 306–327, DOI: `10.1038/s41570-018-0042-6`.

(6) Stumm, W. Reactivity at the Mineral-Water interface: Dissolution and Inhibition. *Colloids Surface A* **1997**, *120*, 143–166, DOI: `10.1016/S0927-7757(96)03866-6`.

(7) Pöschl, U.; Shiraiwa, M. Multiphase Chemistry at the Atmosphere–Biosphere Interface Influencing Climate and Public Health in the Anthropocene. *Chem. Rev.* **2015**, *115*, 4440–4475, DOI: `10.1021/cr500487s`.

(8) Schill, S. R.; Collins, D. B.; Lee, C.; Morris, H. S.; Novak, G. A.; Prather, K. A.; Quinn, P. K.; Sultana, C. M.; Tivanski, A. V.; Zimmermann, K. *et al.* The Impact of Aerosol Particle Mixing State on the Hygroscopicity of Sea Spray Aerosol. *ACS Cent. Sci.* **2015**, *1*, 132–141, DOI: `10.1021/acscentsci.5b00174`.

(9) McCluskey, C. S.; Hill, T. C. J.; Malfatti, F.; Sultana, C. M.; Lee, C.; Santander, M. V.; Beall, C. B.; Moore, K. A.; Cornwell, G. C.; Collins, D. B. *et al.* A Dynamic Link between Ice Nucleating Particles Released in Nascent Sea Spray Aerosol and Oceanic Biological Activity during Two Mesocosm Experiments. *J. Atmos. Sci.* **2017**, *74*, 151–166, DOI: `10.1175/JAS-D-16-0087.1`.

(10) Masson-Delmotte, V.; Zhai, P.; Pirani, A.; Connors, S. L.; Péan, C.; Berger, S.; Caud, N.; Chen, L., Y. Goldfarb; Gomis, M. I.; Huang, M. *et al. IPCC, 2021: Climate Change 2021: The Physical Science Basis. Contribution of Working Group I to the Sixth Assessment Report of the Intergovernmental Panel on Climate Change*; Cambridge University Press, 2021.

(11) Saltzman, E. S. In *Surface Ocean–Lower Atmosphere Processes*; Quéré, C. L., Saltzman, E. S., Eds.; American Geophysical Union (AGU), 2009; pp 17–35, DOI: `10.1029/2008GM000769`.

(12) Herrmann, H.; Schaefer, T.; Tilgner, A.; Styler, S. A.; Weller, C.; Teich, M.; Otto, T. Tropospheric Aqueous-Phase Chemistry: Kinetics, Mechanisms, and Its Coupling to a Changing Gas Phase. *Chem. Rev.* **2015**, *115*, 4259–4334, DOI: `10.1021/cr500447k`.

(13) Quinn, P. K.; Collins, D. B.; Grassian, V. H.; Prather, K. A.; Bates, T. S. Chemistry and Related Properties of Freshly Emitted Sea Spray Aerosol. *Chem. Rev.* **2015**, *115*, 4383–4399, DOI: `10.1021/cr500713g`.

(14) Bertram, T. H.; Cochran, R. E.; Grassian, V. H.; Stone, E. A. Sea Spray Aerosol Chemical Composition: Elemental and Molecular Mimics for Laboratory Studies of Heterogeneous and Multiphase Reactions. *Chem. Soc. Rev.* **2018**, *47*, 2374–2400, DOI: `10.1039/C7CS00008A`.

(15) Aller, J. Y.; Kuznetsova, M. R.; Jahns, C. J.; Kemp, P. F. The Sea Surface Microlayer

as a Source of Viral and bacterial Enrichment in Marine Aerosols. *J. Aerosol Sci.* **2005**, *36*, 801–812, DOI: `10.1016/j.jaerosci.2004.10.012`.

(16) Farmer, D. K.; Cappa, C. D.; Kreidenweis, S. M. Atmospheric Processes and Their Controlling Influence on Cloud Condensation Nuclei Activity. *Chem. Rev.* **2015**, *115*, 4199–4217, DOI: `10.1021/cr5006292`.

(17) Bates, T. S.; Huebert, B. J.; Gras, J. L.; Griffiths, F. B.; Durkee, P. A. International Global Atmospheric Chemistry (IGAC) Project's First Aerosol Characterization Experiment (ACE 1): Overview. *J. Geophys. Res. Atmos.* **1998**, *103*, 16297–16318, DOI: `10.1029/97JD03741`.

(18) Zhang, X.; Massoli, P.; Quinn, P. K.; Bates, T. S.; Cappa, C. D. Hygroscopic Growth of Submicron and Supermicron Aerosols in the Marine Boundary Layer. *J. Geophys. Res. Atmos.* **2014**, *119*, 8384–8399, DOI: `10.1002/2013JD021213`.

(19) Björneholm, O.; Hansen, M. H.; Hodgson, A.; Liu, L.-M.; Limmer, D. T.; Michaelides, A.; Pedevilla, P.; Rossmeisl, J.; Shen, H.; Tocci, G. *et al.* Water at Interfaces. *Chem. Rev.* **2016**, *116*, 7698–7726, DOI: `10.1021/acs.chemrev.6b00045`.

(20) Mucha, M.; Frigato, T.; Levering, L. M.; Allen, H. C.; Tobias, D. J.; Dang, L. X.; Jungwirth, P. Unified Molecular Picture of the Surfaces of Aqueous Acid, Base, and Salt Solutions. *J. Phys. Chem. B.* **2005**, *109*, 7617–7623, DOI: `10.1021/jp0445730`.

(21) Ishiyama, T.; Morita, A. Molecular Dynamics Study of Gas-Liquid Aqueous Sodium Halide Interfaces. I. Flexible and Polarizable Molecular Modeling and Interfacial Properties. *J. Phys. Chem. C* **2007**, *111*, 721–737, DOI: `10.1021/jp065191s`.

(22) D'Auria, R.; Tobias, D. J. Relation between Surface Tension and Ion Adsorption at the Air-Water Interface: A Molecular Dynamics Simulation Study. *J. Phys. Chem. A* **2009**, *113*, 7286–7293, DOI: `10.1021/jp810488p`.

(23) Ottosson, N.; Heyda, J.; Wernersson, E.; Pokapanich, W.; Svensson, S.; Winter, B.; Öhrwall, G.; Jungwirth, P.; Björneholm, O. The Influence of Concentration on the Molecular Surface Structure of Simple and Mixed Aqueous Electrolytes. *Phys. Chem. Chem. Phys.* **2010**, *12*, 10693–10700, DOI: `10.1039/C0CP00365D`.

(24) Hammerich, A. D.; Buch, V. Ab Initio Molecular Dynamics Simulations of the Liquid/Vapor Interface of Sulfuric Acid Solutions. *J. Phys. Chem. A* **2012**, *116*, 5637–5652, DOI: `10.1021/jp2126398`.

(25) Cummings, O. T.; Wick, C. D. Interfacial Behavior of Simple Inorganic Salts at the Air-Water Interface Investigated with a Polarizable Model with Electrostatic Damping. *J. Chem. Phys.* **2013**, *139*, 064708, DOI: `10.1063/1.4817775`.

(26) Neyt, J.-C.; Wender, A.; Lachet, V.; Ghoufi, A.; Malfreyt, P. Prediction of the Concentration Dependence of the Surface Tension and Density of Salt Solutions: Atomistic Simulations using Drude Oscillator Polarizable and Nonpolarizable Models. *Phys. Chem. Chem. Phys.* **2013**, *15*, 11679–11690, DOI: `10.1039/C3CP50904D`.

(27) Baer, M. D.; Tobias, D. J.; Mundy, C. J. Investigation of Interfacial and Bulk Dissociation of HBr, HCl, and HNO_3 Using Density Functional Theory-Based Molecular Dynamics Simulations. *J. Phys. Chem. C* **2014**, *118*, 29412–29420, DOI: `10.1021/jp5062896`.

(28) Murdachaew, G.; Nathanson, G. M.; Benny Gerber, R.; Halonen, L. Deprotonation of Formic Acid in Collisions with a Liquid Water Surface Studied by Molecular Dynamics and Metadynamics Simulations. *Phys. Chem. Chem. Phys.* **2016**, *18*, 29756–29770, DOI: `10.1039/C6CP06071D`.

(29) Olivieri, G.; Parry, K. M.; D'Auria, R.; Tobias, D. J.; Brown, M. A. Specific Anion Effects on Na^+ Adsorption at the Aqueous Solution-Air Interface: MD Simulations,

SESSA Calculations, and Photoelectron Spectroscopy Experiments. *J. Phys. Chem. B* **2018**, *122*, 910–918, DOI: `10.1021/acs.jpcb.7b06981`.

(30) Luo, Y.; Jiang, W.; Yu, H.; MacKerell, A. D.; Roux, B. Simulation Study of Ion Pairing in Concentrated Aqueous Salt Solutions with a Polarizable Force Field. *Faraday Discuss.* **2013**, *160*, 135–149, DOI: `10.1039/C2FD20068F`.

(31) Soniat, M.; Pool, G.; Franklin, L.; Rick, S. W. Ion Association in Aqueous Solution. *Fluid Phase Equil.* **2016**, *407*, 31–38, DOI: `10.1016/j.fluid.2015.05.001`, Aqueous Solutions.

(32) Xu, P.; Guidez, E. B.; Bertoni, C.; Gordon, M. S. Perspective: Ab initio Force Field Methods Derived from Quantum Mechanics. *J. Chem. Phys.* **2018**, *148*, 090901, DOI: `10.1063/1.5009551`.

(33) Gránásy, L. Semiempirical van der Waals/Cahn-Hilliard Theory: Size Dependence of the Tolman Length. *J. Chem. Phys.* **1998**, *109*, 9660–9663, DOI: `10.1063/1.477634`.

(34) Liu, H.; Cao, G. Effectiveness of the Young-Laplace Equation at Nanoscale. *Scientific Reports* **2016**, *6*, 23936, DOI: `10.1038/srep23936`.

(35) Montero de Hijes, P.; Espinosa, J. R.; Bianco, V.; Sanz, E.; Vega, C. Interfacial Free Energy and Tolman Length of Curved Liquid–Solid Interfaces from Equilibrium Studies. *J. Phys. Chem. C* **2020**, *124*, 8795–8805, DOI: `10.1021/acs.jpcc.0c00816`.

(36) Kashchiev, D. Nucleation Work, Surface Tension, and Gibbs-Tolman Length for Nucleus of any Size. *J. Chem. Phys.* **2020**, *153*, 124509, DOI: `10.1063/5.0021337`.

(37) de Miguel, R.; Rubí, J. M. Gibbs Thermodynamics and Surface Properties at the Nanoscale. *J. Chem. Phys.* **2021**, *155*, 221101, DOI: `10.1063/5.0072533`.

(38) Tolman, R. C. The Effect of Droplet Size on Surface Tension. *J. Chem. Phys.* **1949**, *17*, 333–337, DOI: `10.1063/1.1747247`.

(39) Köhler, H. The Nucleus in and the Growth of Hygroscopic Droplets. *Trans. Faraday Soc.* **1936**, *32*, 1152–1161, DOI: `10.1039/TF9363201152`.

(40) McGraw, R.; Laaksonen, A. Scaling Properties of the Critical Nucleus in Classical and Molecular-Based Theories of Vapor-Liquid Nucleation. *Phys. Rev. Lett.* **1996**, *76*, 2754–2757, DOI: `10.1103/PhysRevLett.76.2754`.

(41) Kashchiev, D. Determining the Curvature Dependence of Surface Tension. *J. Chem. Phys.* **2003**, *118*, 9081–9083, DOI: `10.1063/1.1576218`.

(42) Joswiak, M. N.; Duff, N.; Doherty, M. F.; Peters, B. Size-Dependent Surface Free Energy and Tolman-Corrected Droplet Nucleation of TIP4P/2005 Water. *J. Phys. Chem. Lett.* **2013**, *4*, 4267–4272, DOI: `10.1021/jz402226p`.

(43) Factorovich, M. H.; Molinero, V.; Scherlis, D. A. Vapor Pressure of Water Nanodroplets. *Journal of the American Chemical Society* **2014**, *136*, 4508–4514, DOI: `10.1021/ja405408n`.

(44) Leong, K.-Y.; Wang, F. A Molecular Dynamics Investigation of the Surface Tension of Water Nanodroplets and a New Technique for Local Pressure Determination through Density Correlation. *J. Chem. Phys.* **2018**, *148*, 144503, DOI: `10.1063/1.5004985`.

(45) Moody, M. P.; Attard, P. Curvature-Dependent Surface Tension of a Growing Droplet. *Phys. Rev. Lett.* **2003**, *91*, 056104, DOI: `10.1103/PhysRevLett.91.056104`.

(46) Wilhelmsen, O.; Bedeaux, D.; Reguera, D. Tolman Length and Rigidity Constants of the Lennard-Jones Fluid. *J. Chem. Phys.* **2015**, *142*, 064706, DOI: `10.1063/1.4907588`.

(47) Zhong, J.; Riordon, J.; Zandavi, S. H.; Xu, Y.; Persad, A. H.; Mostowfi, F.; Sinton, D. Capillary Condensation in 8 nm Deep Channels. *J. Phys. Chem. Lett.* **2018**, *9*, 497–503, DOI: `10.1021/acs.jpclett.7b03003`, PMID: 29323911.

(48) Réal, F.; Vallet, V.; Flament, J.-P.; Masella, M. Revisiting a Many-Body Model for Water Based on a Single Polarizable Site. From Gas Phase Clusters to Liquid and Air/Liquid Water Systems. *J. Chem. Phys.* **2013**, *139*, 114502.

(49) Réal, F.; Gomes, A. S. P.; Guerrero Martinez, Y. O.; Ayed, T.; Galland, N.; Masella, M.; Vallet, V. Structural, Dynamical, and Transport Properties of the Hydrated Halides: How Do At^- and I^- Bulk Properties Compare with those of the other Halides, from F^- to I^-. *J. Chem. Phys.* **2016**, *144*, 124513, DOI: `10.1063/1.4944613`.

(50) Réal, F.; Vallet, V.; Masella, M. Improving the Description of Solvent Pairwise Interactions using Local Solute/Solvent Three-Body Functions. The Case of Halides and Carboxylates in Aqueous Environments. *J. Comput. Chem.* **2019**, *40*, 1209–1218, DOI: `10.1002/jcc.25779`.

(51) Houriez, C.; Réal, F.; Vallet, V.; Mautner, M.; Masella, M. Ion Hydration Free Energies and Water Surface Potential in Water nano Drops: The Cluster Pair Approximation and the Proton Hydration Gibbs Free Energy in Solution. *J. Chem. Phys.* **2019**, *151*, 174504, DOI: `10.1063/1.5109777`.

(52) Debiec, K. T.; Gronenborn, A. M.; Chong, L. T. Evaluating the Strength of Salt Bridges: A Comparison of Current Biomolecular Force Fields. *J. Phys. Chem. B* **2014**, *118*, 6561–6569, DOI: `10.1021/jp500958r`.

(53) Thole, B. Molecular Polarizabilities Calculated with a Modified Dipole Interaction. *Chem. Phys.* **1981**, *59*, 341–350.

(54) Trumm, M.; Guerrero Martinez, Y. O.; Réal, F.; Schimmelpfennig, B.; Masella, M.; Vallet, V. Modeling the Hydration of Mono-Atomic Anions From the Gas Phase to the Bulk Phase: The Case of the Halide Ions F^-, Cl^-, and Br^-. *J. Chem. Phys.* **2012**, *136*, 044509, DOI: `10.1063/1.3678294`.

(55) Houriez, C.; Meot-Ner (Mautner), M.; Masella, M. Simulated Solvation of Organic Ions II: Study of Linear Alkylated Carboxylate Ions in Water Nanodrops and in Liquid Water. Propensity for Air/Water Interface and Convergence to Bulk Solvation Properties. *J. Phys. Chem. B* **2015**, *119*, 12094–12107, DOI: `10.1021/acs.jpcb.5b04556`.

(56) Rogers, D. M.; Beck, T. L. Quasichemical and Structural Analysis of Polarizable Anion Hydration. *J. Chem. Phys.* **2010**, *132*, 014505, DOI: `10.1063/1.3280816`.

(57) Houriez, C.; Meot-Ner (Mautner), M.; Masella, M. Simulated Solvation of Organic Ions: Protonated Methylamines in Water Nanodroplets. Convergence toward Bulk Properties and the Absolute Proton Solvation Enthalpy. *J. Phys. Chem. B* **2014**, *118*, 6222–6233, DOI: `10.1021/jp501630q`.

(58) Galib, M.; Baer, M. D.; Skinner, L. B.; Mundy, C. J.; Huthwelker, T.; Schenter, G. K.; Benmore, C. J.; Govind, N.; Fulton, J. L. Revisiting the Hydration Structure of Aqueous Na^+. *J. Chem. Phys.* **2017**, *146*, 084504, DOI: `10.1063/1.4975608`.

(59) Werner, H.-J.; Knowles, P. J.; Knizia, G.; Manby, F. R.; Schütz, M. Molpro: a general-purpose quantum chemistry program package. *WIREs Comput Mol Sci* **2012**, *2*, 242–253.

(60) Werner, H.-J.; Knowles, P. J.; Knizia, G.; Manby, F. R.; Schütz, M.; Celani, P.; Györffy, W.; Kats, D.; Korona, T.; Lindh, R. *et al.* MOLPRO, version 2019.1, a package of ab initio programs. see https://www.molpro.net.

(61) http://biodev.cea.fr/polaris/.

(62) Masella, M. The Multiple Time Step r-RESPA Procedure and Polarizable Potentials Based on Induced Dipole Moments. *Mol. Phys.* **2006**, *104*, 415–428.

(63) Liu, Y.; Tuckerman, M. Generalized Gaussian Moment Thermostatting: A New Con-

tinuous Dynamical Approach to the Canonical Ensemble. *J. Chem. Phys.* **2000**, *112*, 1685–1700.

(64) Coles, J. P.; Masella, M. The Fast Multipole Method and Point Dipole Moment Polarizable Force Fields. *J. Chem. Phys.* **2015**, *142*, 024109, DOI: `10.1063/1.4904922`.

(65) Toukmaji, A.; Sagui, C.; Borad, J.; Darden, T. Efficient Particle-Mesh Ewald Based Approach to Fixed and Induced Dipolar Interactions. *J. Chem. Phys.* **2000**, *113*, 10913–10927.

(66) Houriez, C.; Vallet, V.; Réal, F.; Meot-Ner (Mautner), M.; Masella, M. Organic Ion Association in Aqueous Phase and Ab Initio-Based Force Fields: The Case of Carboxylate/Ammonium Salts. *J. Chem. Phys.* **2017**, *147*, 161720, DOI: `10.1063/1.4997996`.

(67) Timko, J.; Bucher, D.; Kuyucak, S. Dissociation of NaCl in Water from Ab Initio Molecular Dynamics Simulations. *J. Chem. Phys.* **2010**, *132*, 114510, DOI: `10.1063/1.3360310`.

(68) Pliego, J. R. The Role of Intermolecular Forces in Ionic Reactions: the Solvent Effect, Ion-Pairing, Aggregates and Structured Environment. *Org. Biomol. Chem.* **2021**, *19*, 1900–1914, DOI: `10.1039/D0OB02413A`.

(69) Fennell, C. J.; Bizjak, A.; Vlachy, V.; Dill, K. A. Ion Pairing in Molecular Simulations of Aqueous Alkali Halide Solutions. *J. Phys. Chem. B* **2009**, *113*, 6782–6791, DOI: `10.1021/jp809782z`.

(70) Kelley, M.; Donley, A.; Clark, S.; Clark, A. Structure and Dynamics of NaCl Ion Pairing in Solutions of Water and Methanol. *J. Phys. Chem. B* **2015**, *119*, 15652–15661, DOI: `10.1021/acs.jpcb.5b07492`.

(71) Wills, A.; Fernández-Serra, M. Role of Water Model on Ion Dissociation at Ambient Conditions. *J. Chem. Phys.* **2021**, *154*, 194502, DOI: `10.1063/5.0046188`.

(72) Aveyard, R.; Saleem, S. M. Interfacial Tensions at Alkane-Aqueous Electrolyte Interfaces. *J. Chem. Soc., Faraday Trans. 1* **1976**, *72*, 1609–1617, DOI: `10.1039/F19767201609`.

(73) Knipping, E. M.; Lakin, M. J.; Foster, K. L.; Jungwirth, P.; Tobias, D. J.; Gerber, R. B.; Dabdub, D.; Finlayson-Pitts, B. J. Experiments and Simulations of Ion-Enhanced Interfacial Chemistry on Aqueous NaCl Aerosols. *Science* **2000**, *288*, 301–306, DOI: `10.1126/science.288.5464.301`.

(74) Tian, C.; Byrnes, S. J.; Han, H.-L.; Shen, Y. R. Surface Propensities of Atmospherically Relevant Ions in Salt Solutions Revealed by Phase-Sensitive Sum Frequency Vibrational Spectroscopy. *J. Phys. Chem. Lett.* **2011**, *2*, 1946–1949, DOI: `10.1021/jz200791c`.

(75) Piatkowski, L.; Zhang, Z.; Backus, E. H. G.; Bakker, H. J.; Bonn, M. Extreme Surface Propensity of Halide Ions in Water. *Nat. Commun.* **2014**, *5*, 4083, DOI: `10.1038/ncomms5083`.

(76) Ho, C.-H.; Tsao, H.-K.; Sheng, Y.-J. Interfacial Tension of a Salty Droplet: Monte Carlo Study. *J. Chem. Phys.* **2003**, *119*, 2369–2375, DOI: `10.1063/1.1587128`.

(77) Shah, A. A.; Ali, K.; Bilal, S. Surface Tension, Surface Excess Concentration, Enthalpy and Entropy of Surface Formation of Aqueous Salt Solutions. *Colloid. Surface A* **2013**, *417*, 183–190, DOI: `10.1016/j.colsurfa.2012.10.054`.

(78) Underwood, T. R.; Greenwell, H. C. The Water-Alkane Interface at Various NaCl Salt Concentrations: A Molecular Dynamics Study of the Readily Available Force Fields. *Sci. Rep.* **2018**, *8*, 352, DOI: `10.1038/s41598-017-18633-y`.

(79) Degrève, L.; da Silva, F. L. B. Structure of concentrated aqueous NaCl solution: A Monte Carlo study. *J. Chem. Phys.* **1999**, *110*, 3070–3078, DOI: `10.1063/1.477903`.

(80) Uchida, H.; Matsuoka, M. Molecular Dynamics Simulation of Solution Structure and Dynamics of Aqueous Sodium Chloride Solutions from Dilute to Supersaturated Concentration. *Fluid Phase Equil.* **2004**, *219*, 49–54, DOI: `10.1016/j.fluid.2004.01.013`.

(81) Fedkin, M. V.; Shin, Y. K.; Dasgupta, N.; Yeon, J.; Zhang, W.; van Duin, D.; van Duin, A. C. T.; Mori, K.; Fujiwara, A.; Machida, M. *et al.* Development of the ReaxFF Methodology for Electrolyte-Water Systems. *J. Phys. Chem. A* **2019**, *123*, 2125–2141, DOI: `10.1021/acs.jpca.8b10453`.

(82) Hassan, S. A. Morphology of Ion Clusters in Aqueous Electrolytes. *Phys. Rev. E* **2008**, *77*, 031501, DOI: `10.1103/PhysRevE.77.031501`.

(83) Hassan, S. A. Computer Simulation of Ion Cluster Speciation in Concentrated Aqueous Solutions at Ambient Conditions. *J. Phys. Chem. B* **2008**, *112*, 10573–10584, DOI: `10.1021/jp801147t`.

(84) Georgalis, Y.; Kierzek, A. M.; Saenger, W. Cluster Formation in Aqueous Electrolyte Solutions Observed by Dynamic Light Scattering. *J. Phys. Chem. B* **2000**, *104*, 3405–3406, DOI: `10.1021/jp000132e`.

(85) Samal, S.; Geckeler, K. E. Unexpected Solute Aggregation in Water on Dilution. *Chem. Commun.* **2001**, 2224–2225, DOI: `10.1039/B105399J`.

(86) Bharmoria, P.; Gupta, H.; Mohandas, V. P.; Ghosh, P. K.; Kumar, A. Temperature Invariance of NaCl Solubility in Water: Inferences from Salt-Water Cluster Behavior of NaCl, KCl, and NH_4Cl. *J. Phys. Chem. B* **2012**, *116*, 11712–11719, DOI: `10.1021/jp307261g`.

(87) Konovalov, A. I.; Ryzhkina, I. S. Highly Diluted Aqueous Solutions: Formation of Nano-Sized Molecular Assemblies (Nanoassociates). *Geochem. Int.* **2014**, *52*, 1207–1226, DOI: `10.1134/S0016702914130072`.

(88) Lanaro, G.; Patey, G. N. Birth of NaCl Crystals: Insights from Molecular Simulations. *J. Phys. Chem. B* **2016**, *120*, 9076–9087, DOI: `10.1021/acs.jpcb.6b05291`.

(89) Lamoureux, G.; Roux, B. Absolute Hydration Free Energy Scale for Alkali and Halide Ions Established from Simulations with a Polarizable Force Field. *J. Phys. Chem. B* **2006**, *110*, 3308–3322, DOI: `10.1021/jp056043p`.

(90) Jarvis, N. L.; Scheiman, M. A. Surface Potentials of Aqueous Electrolyte Solutions. *J. Phys. Chem.* **1968**, *72*, 74–78, DOI: `10.1021/j100847a014`.

(91) Adel, T.; Velez-Alvarez, J.; Co, A. C.; Allen, H. C. Circuit Analysis of Ionizing Surface Potential Measurements of Electrolyte Solutions. *J. Electrochem. Soc.* **2021**, *168*, 016507, DOI: `10.1149/1945-7111/abd649`.

(92) Johansson, K.; Eriksson, J. C. γ and dγ/dT Measurements on Aqueous Solutions of 1,1-Electrolytes. *Journal of Colloid and Interface Science* **1974**, *49*, 469–480, DOI: `10.1016/0021-9797(74)90393-2`.

(93) Alekseechkin, N. V. Tolman Length and Limiting Supersaturation of Vapor. *Chemical Physics* **2018**, *500*, 19–25, DOI: `10.1016/j.chemphys.2017.11.007`.

(94) Tröster, A.; Oettel, M.; Block, B.; Virnau, P.; Binder, K. Numerical Approaches to Determine the Interface Tension of Curved Interfaces from Free energy Calculations. *J. Chem. Phys.* **2012**, *136*, 064709, DOI: `10.1063/1.3685221`.

(95) Bruot, N.; Caupin, F. Curvature Dependence of the Liquid-Vapor Surface Tension beyond the Tolman Approximation. *Phys. Rev. Lett.* **2016**, *116*, 056102, DOI: `10.1103/PhysRevLett.116.056102`.

(96) https://hal.archives-ouvertes.fr/hal-03019154.

Supporting Information

NaCl salts in finite aqueous environments at the fine particle marine aerosol scale.

Valérie Vallet,[†] Jonathan Coles,[‡] Florent Réal,[†] Céline Houriez,[¶] and Michel Masella[*,§]

[†]*Univ. Lille, CNRS, UMR 8523 - PhLAM - Physique des Lasers Atomes et Molécules, F-59000 Lille, France*

[‡]*Leibniz Supercomputing Centre of the Bavarian Academy of Sciences and Humanities (LRZ), Boltzmannstrasse 1, Garching b. München, D-85748 Garching, Germany*

[¶]*MINES ParisTech, PSL Research University, CTP - Centre Thermodynamique des Procédés, 35 rue Saint-Honoré, F-77300 Fontainebleau, France*

[§]*Laboratoire Bioénergétique, Métalloprotéines et Stress, Service de Bioénergétique, Biologie Structurale et Mécanismes, Institut Joliot, CEA Saclay, F-91191 Gif sur Yvette Cedex, France*

E-mail: michel.masella@cea.fr

Short range many body functions to improve the force field reliability regarding large ion/water clusters : their effect on NaCL PMF in neat water

To improve the accuracy of our force fields to model

- the large hydrated halide anion clusters (comprising more than 6 water molecules) that can be observed in aqueous environments (up to 12 water molecules can accommodate in the first hydration shell of halides and carboxylate anions);
- alkali/water clusters presenting a partial or complete second hydration shell,

we built up specific short range many-body functions (denoted as U^{sc}), whose analytical form is close to the U^{coop} one to model hydrogen bonds. These functions U^{sc} improve the modeling of water/water interactions only at the close vicinity of anionic and cationic centers. For the present purpose, we used the U^{sc} functions (and their parameters) allowing one to model the hydration of Na^+ and Cl^- from our earlier studies[1,2]. The $U^{sc}(\mathrm{Cl}^-)$ and $U^{sc}(\mathrm{Na}^+)$ functions destabilize and stabilize the ion/water interactions in large hydrated ionic clusters, respectively.

We plot in Figure S1 the $[\mathrm{Na}^+, \mathrm{Cl}^-]$ PMF in liquid water computed from our polarizable force-field approach, as well as the PMFs computed by omitting both the correction potentials $U^{sc}(\mathrm{Cl}^-)$ and $U^{sc}(\mathrm{Na}^+)$ and only a single one. The latter four PMFs are denoted $\mathrm{PMF}^{\mathrm{full}}$, $\mathrm{PMF}^{\mathrm{nosc}}$, $\mathrm{PMF}^{\mathrm{nosc(Na^+)}}$ and $\mathrm{PMF}^{\mathrm{nosc(Cl^-)}}$, respectively. All our PMFs agree with the standard locations of the CIP, TS and SSIP states. Not accounting for both the correction potentials $U^{sc}(\mathrm{Cl}^-)$ and $U^{sc}(\mathrm{Na}^+)$ yields a PMF that differs noticeably from those computed by accounting for these potentials as well as from the CPMD and Drude-based ones discussed in the main manuscript. In that case the energy depth corresponding to CIP is -2 kcal mol^{-1}, for instance. Neglecting only the correction potential $U^{sc}(\mathrm{Na}^+)$ yields to largely over stabilize the first minium CIP (its energy depth is as low as -3.2 kcal mol^{-1}) whereas neglecting only $U^{sc}(\mathrm{Cl}^-)$ yields a PMF profile that agrees the Drude-based one. These results are in line with the expected effects of our correction potentials: $U^{sc}(\mathrm{Cl}^-)$ is built to destabilize the interactions among the water molecules in the chloride first hydration shell (that yields to favor ion pairing), whereas $U^{sc}(\mathrm{Na}^+)$ aims at reinforcing the interaction among water molecules of the Na^+ first and second hydration shell (and that disfavors ion pairing).

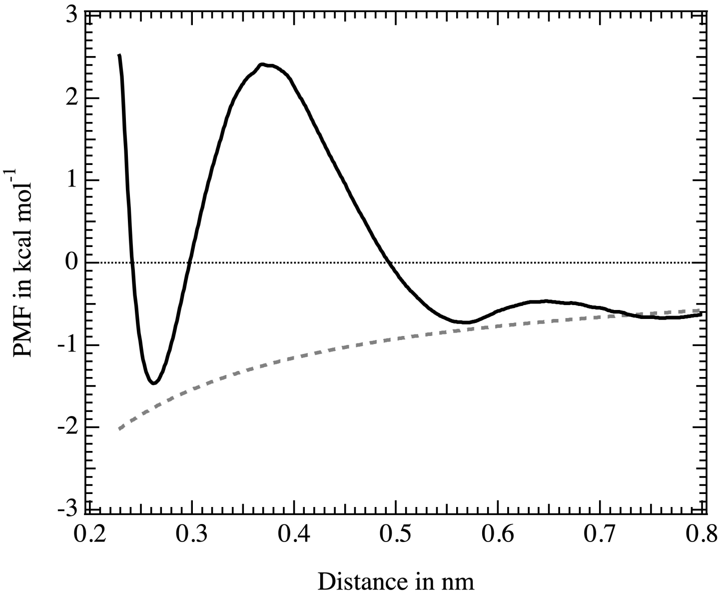

Figure S1: $[\mathrm{Na}^+, \mathrm{Cl}^-]$ ion pair PMFs in neat liquid water at ambient conditions as computed from our force fields. Black ($\mathrm{PMF}^{\mathrm{full}}$) and green lines ($\mathrm{PMF}^{\mathrm{nosc}}$): PMFs computed by accounting for the both the correction potentials $U^{sc}(\mathrm{Cl}^-)$ and $U^{sc}(\mathrm{Na}^+)$ and for none of them, respectively. Blue ($\mathrm{PMF}^{\mathrm{nosc}(\mathrm{Na}^+)}$) and red lines ($\mathrm{PMF}^{\mathrm{nosc}(\mathrm{Cl}^-)}$): PMF computed by accounting only for $U^{sc}(\mathrm{Na}^+)$ and for $U^{sc}(\mathrm{Cl}^-)$, respectively. In dashed grey lines, the expected Coulombic PMF corresponding to two point charges of opposite sign in bulk water at ambient conditions. All the simulated PMFs are shifted to meet the Coulombic PMF value at 0.8 nm.

Computing the surface tension of planar interfaces

To simulate planar liquid/gas phase interface regarding neat water and 0.2 and 0.6m NaCl aqueous solutions, we first generated a 10 ns NPT MD runs of a box comprising about 2000 water molecules and whose dimensions are $(L_x = L, L_y = L, L_z = 2L)$, using periodic boundary conditions at ambient conditions according to the protocol detailed in the main manuscript. The average dimensions $\bar{L}$ corresponding to the last 5 ns segment of the trajectories are computed and new 10 ns NVT simulations are performed from the final snapshots of the NPT trajectories and the new cell dimension sets $(\bar{L}, \bar{L}, 2\bar{L})$. Finally, the final snapshots of the NVT simulations are taken as the starting structures of new 60 ns NVT simulations for which the cell dimensions are $(\bar{L}, \bar{L}, 6\bar{L})$. The simulated systems present thus two liquid/vapor interfaces.

Along the 60 ns NVT simulations and once an initial relaxation phase of 10 ns is achieved, we computed the surface tensions $\gamma(\mathrm{T})$ of liquid water and of 0.2 and 0.6m NaCl aqueous solutions at a temperature $\mathrm{T} = 300$ K by means of the test-area simulation method[3]

$$\gamma(\mathrm{T}) = \left(\frac{\Delta A}{\Delta S}\right)_{N,V,T}, \tag{1}$$

here, ΔA is the change in the free energy for an infinitesimal change in the interfacial area S. The $\gamma(\mathrm{T})$'s are computed according to a Free Energy Perturbation scheme (the sampling interval is 50 fs), with the two perturbed states corresponding to the altered surface area $S_{\pm} = L_x L_y (1 \pm \delta_s)$. x and y are the two dimensions orthogonal to the z-axis (the perturbation is equally applied to both). We set δ_s to 5.10^{-3} as recommend in Ref.[4]. The temporal evolutions of the surface tensions for our planar interfaces are plotted in Figure S2.

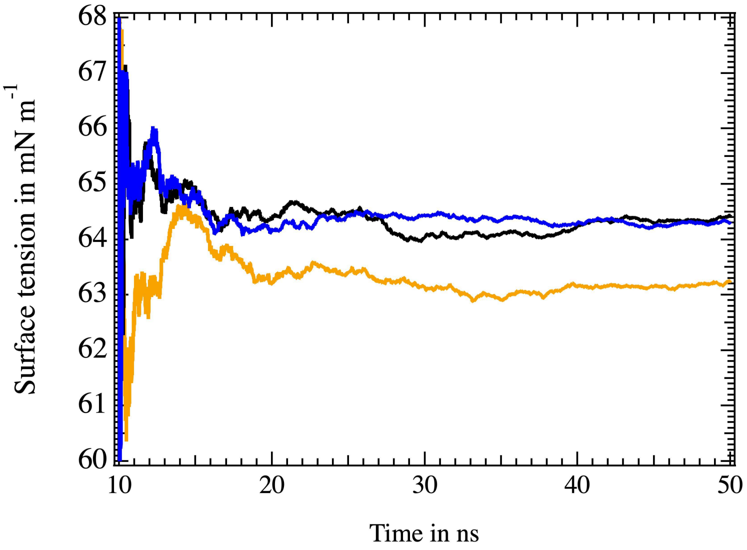

Figure S2: Temporal evolutions of the surface tensions of planar interfaces. Black : 0.6m NaCl solution; blue : 0.2m NaCl solution; orange : neat water.

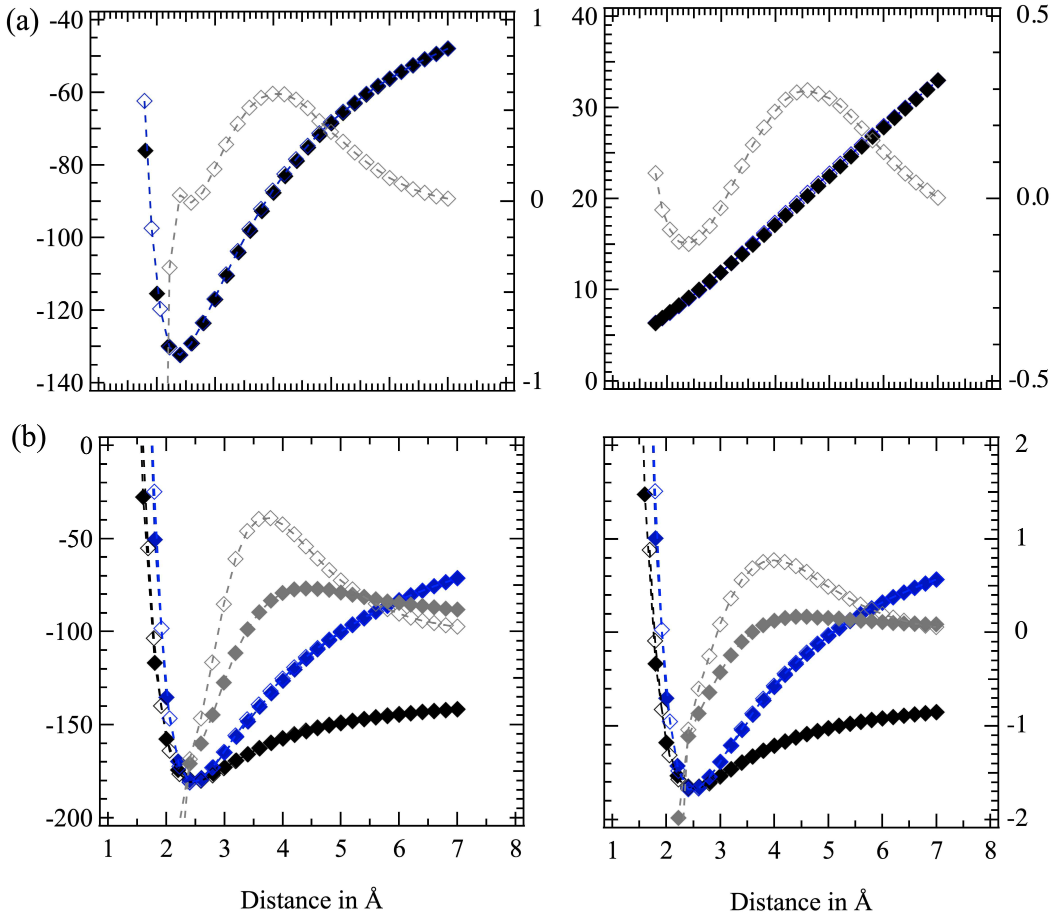

Figure S3: (a) [Na^+, Cl^-] ion pair interaction energy (in kcal mol^{-1}, plot on the left) and total dipole moment (in Debye, plot on the right) in gas phase as a function of the inter ionic distance from *ab initio* MP2/CBS computations (full black symbols) and from our force field (empty blue symbols). Dashed grey lines and symbols: differences between force field and *ab initio* data (right axes). (b) Interaction energies (in kcal mol^{-1}) of the ionic trimers [$(Na^+)_2, Cl^-$] (left) and [$Na^+, (Cl^-)_2$] (right). In these trimers, the single ion is set in between the two ions of opposite charge. Full and empty symbols: quantum and force-field data, respectively. Blue symbols (left axis): trimer interaction energies corresponding to symmetric dissociation of the two charge-like ions. Black symbols (left axis): trimer interaction energies corresponding to the dissociation energy of one of the two charge-like ions. Grey lines and symbols (right axes): force field/quantum differences in the trimer energies.

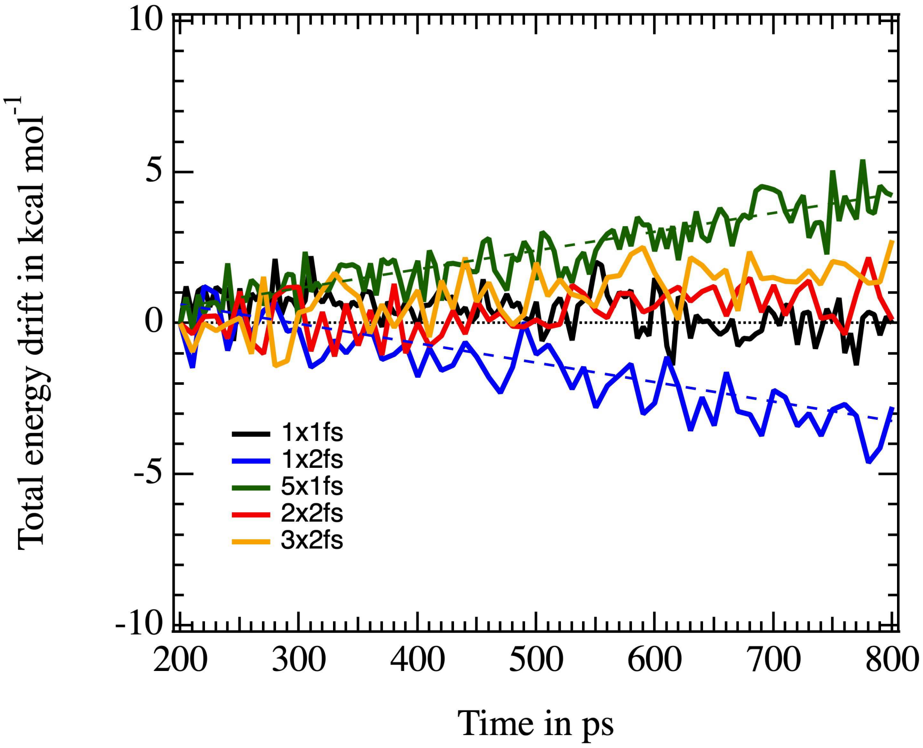

Figure S4: Total energy drifts along 1 ns scale MD simulations in the NVT ensemble at ambient conditions of a cubic box comprising 10 NaCl pairs and about 1000 water molecules. That box is simulated using Particle Mesh Ewald summation techniques, periodic conditions and the polarizable force fields according to the MD protocol detailed in the main manuscript. Here we used five different sets of (X×Y) time steps (in fs) to update the short and long range forces as solving the equations of motion using the r-RESPAp multiple time step scheme, from (1×1 fs) up to (2×6 fs). The temporal evolutions of the energy drift are here all linear on average, the largest slope is about 7 10^{-3} kcal mol^{-1} ps^{-1} in absolute values.

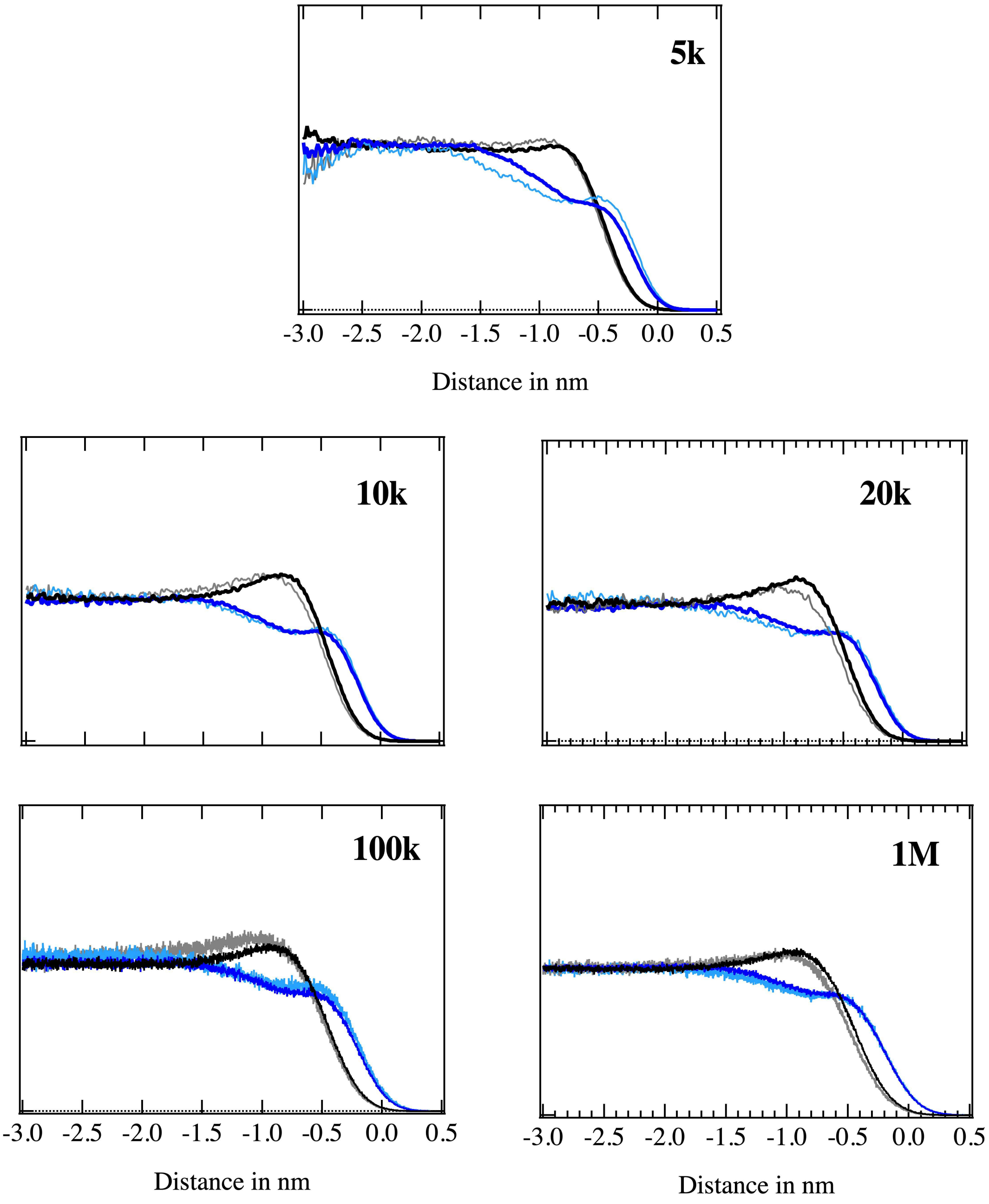

Figure S5: Normalized distributions of ions as a function of their distance from the droplet boundary. From up to down 5k, 10k, 20k, 100k and 1M droplets. Black : Na^+ distributions, blue : Cl^- distributions. Light colors correspond to $0.2m$ droplets.

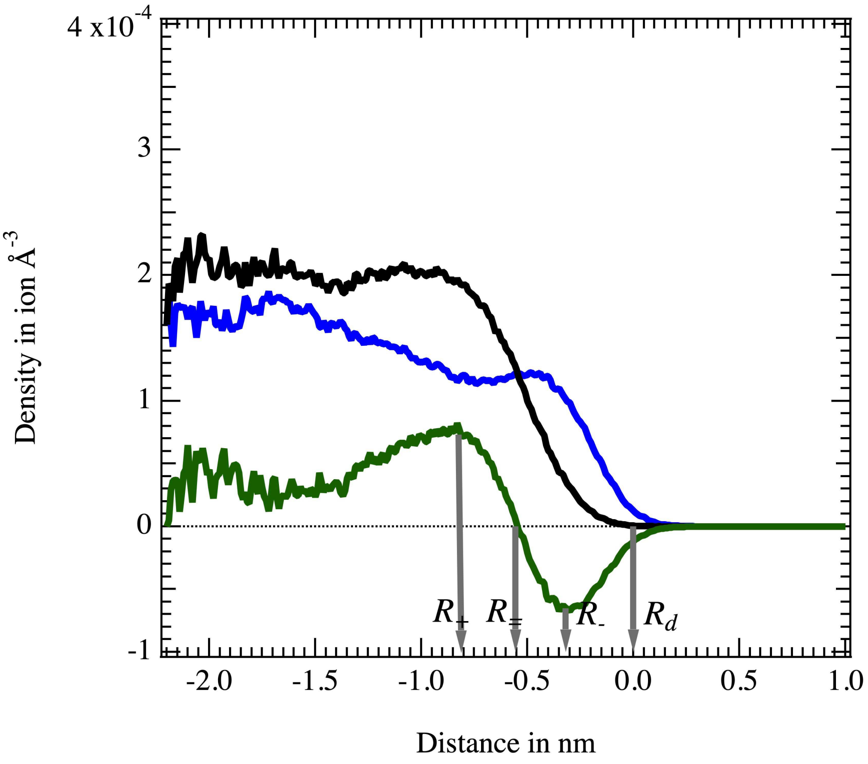

Figure S6: Ion densities as a function of the ion distance from the equi molar radius R_d for the 2k 0.2m droplet. Na$^+$ and Cl$^-$ densities are plotted in black and blue lines, respectively. Green line: difference $\Delta\rho^i(r)$ in the Na$^+$ and Cl$^-$ densities. The vertical grey arrows are located at the minimum, zero and maximum values of the $\Delta\rho^i(r)$ function and at the mean droplet radius R_d.

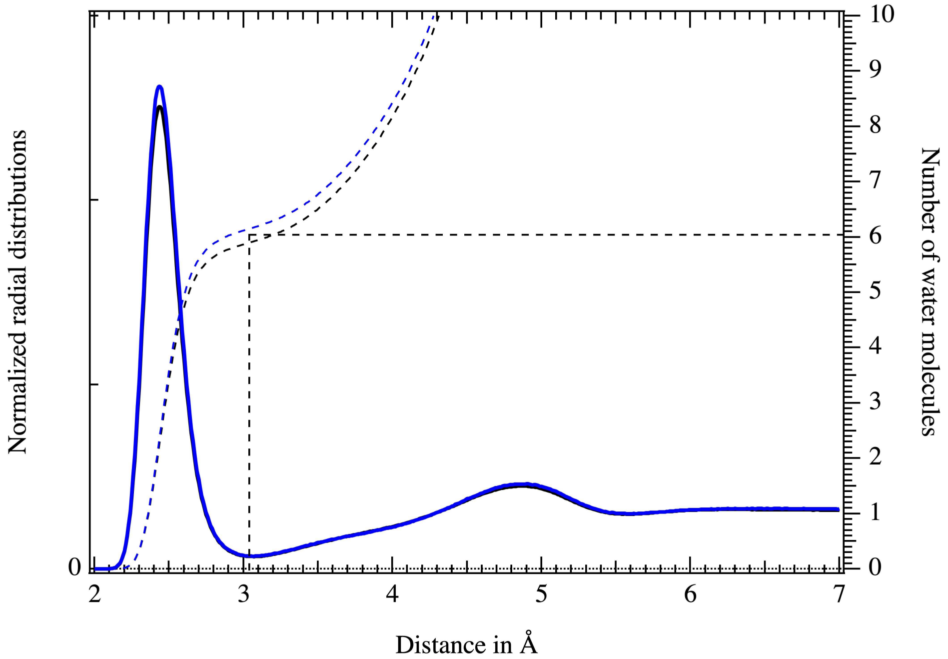

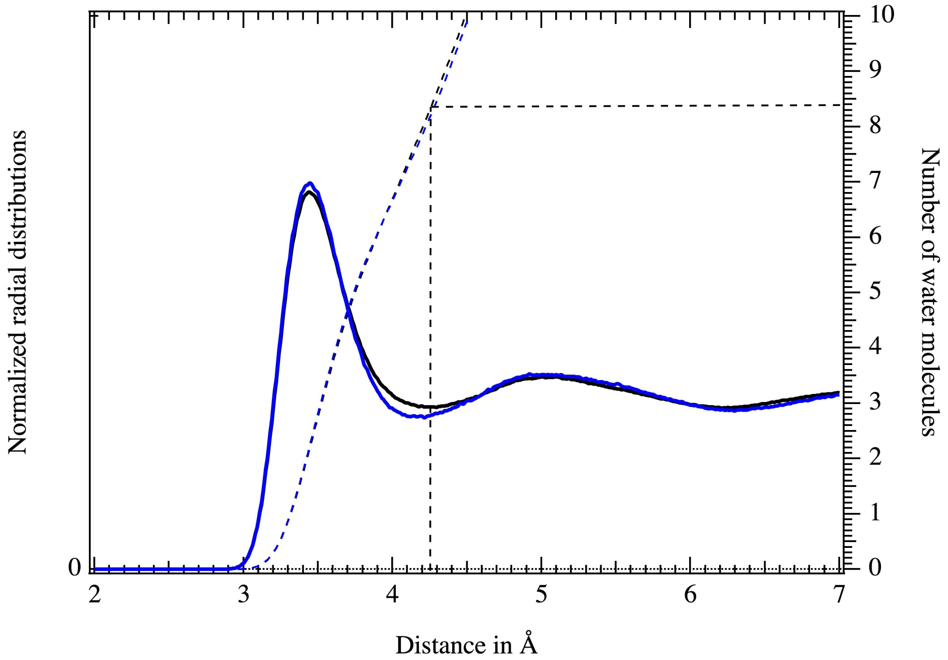

Figure S7: Ion water radial distribution functions (left axes) and their integrals (right axes) as a function of the ion/oxygen distance for the $0.2m$ (blue) and $0.6m$ (black) 10k droplets. Up and down : Na^+ and Cl^- functions, respectively. The uncertainty regarding the position of the second minimum of the distribution functions is about 0.1 Å. That yields an uncertainty regarding the number of water molecules in the ion first coordination sphere that amounts to 0.2 (Na^+) and 0.5 (Cl^-).

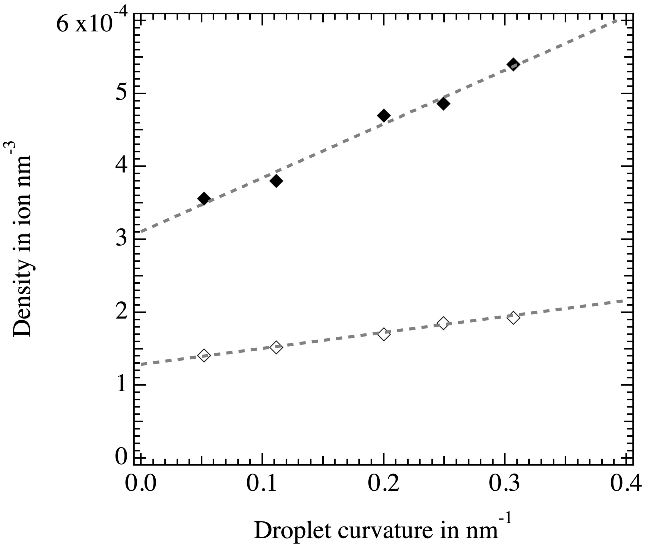

Figure S8: Mean densities $\rho_d^{\mathrm{Na}^+}$ within the droplet bulk-like core domains as a function of the inverse of the droplet radius R_d. Empty and full symbols: 0.2 and 0.6m data, respectively. In dashed line the linear R_d^{-1} functions that best reproduce the densities (the regression coefficients are > 0.98).

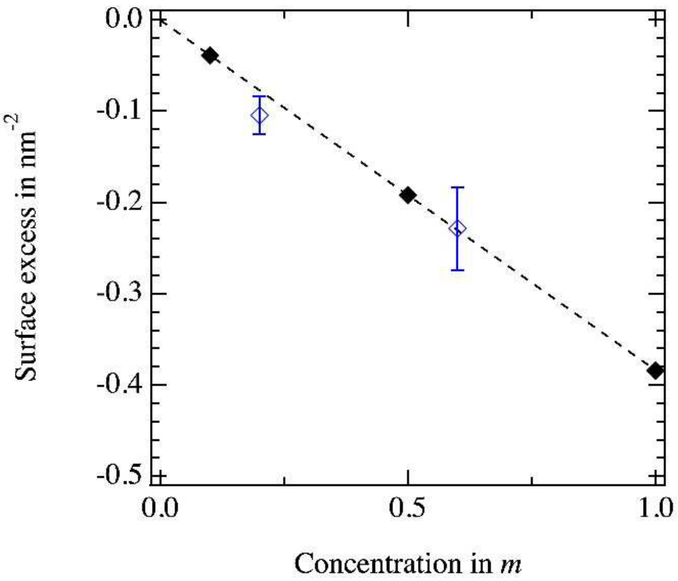

Figure S9: Total ion surface excess values Γ_{tot} as a function of the droplet curvature R_e^{-1}. Blue and black: 0.2 and 0.6m data, respectively; dashed lines: linear regression fits of data corresponding to 10k-1M droplets.

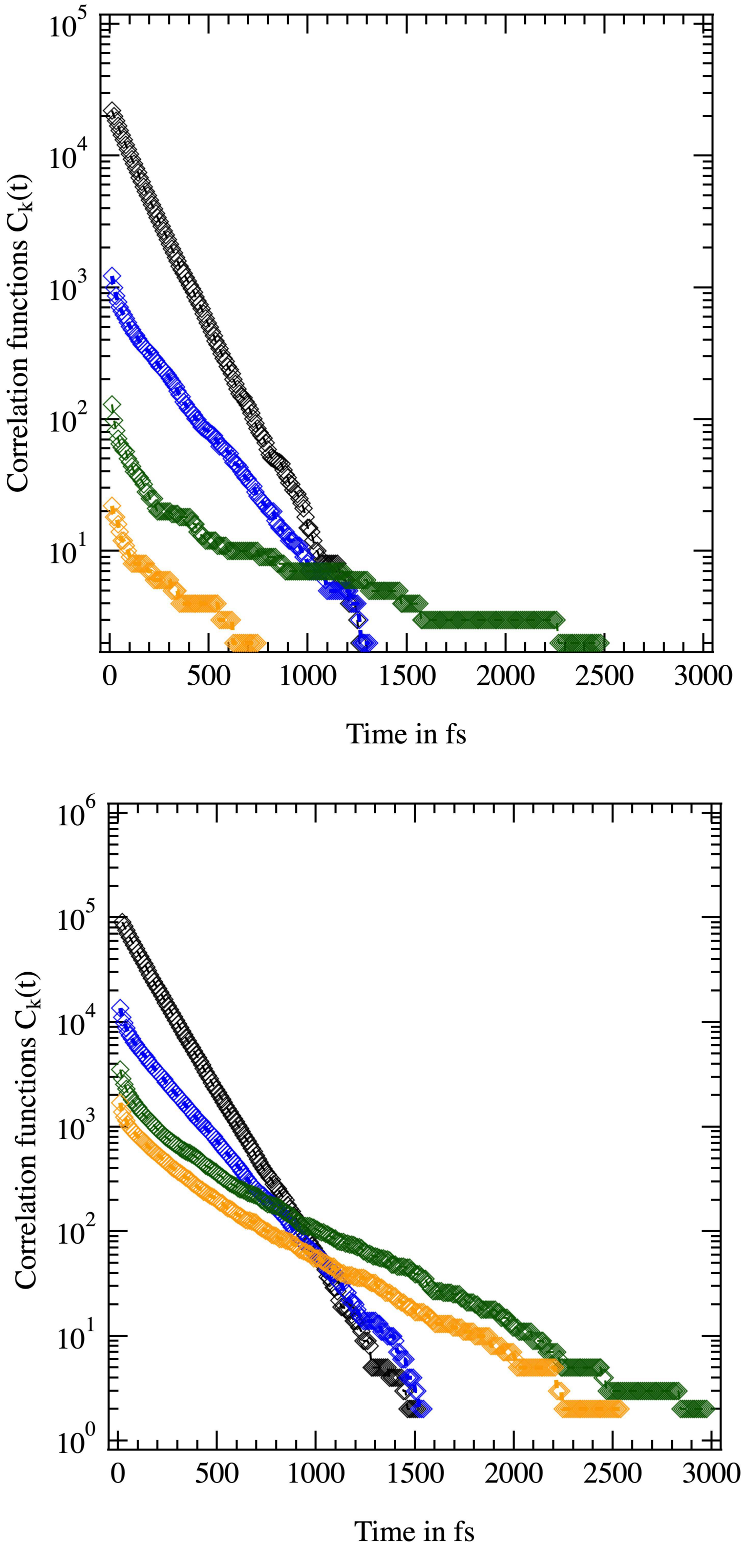

Figure S10: Cluster temporal correlation functions $C_k(t)$. Black, blue, green and orange : data for 2, 3, 4 and 5-sized ion clusters. Up and down : 0.2 and 0.6m data. The linear regression to compute the time τ^* discussed in the main manuscript are performed on the initial segment of the functions.

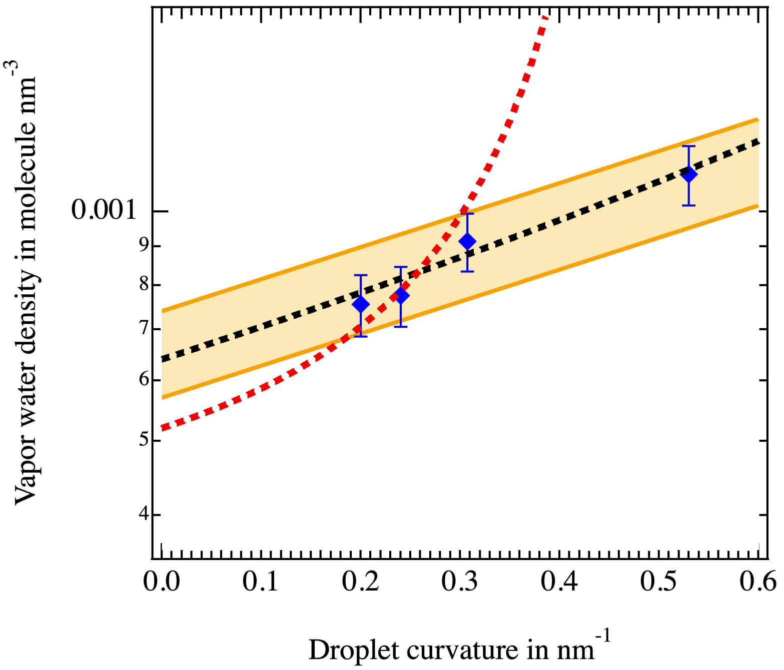

Figure S11: Water vapor density (ln scale) as a function of the droplet curvature R_d^{-1} for pure aqueous droplets whose molecular size ranges from 1k to 20k. Bold dashed line : interpolation of the raw density data according to the Kelvin relation, using a Tolman length value $\delta_\gamma =$ -0.1 nm and a planar interface extrapolated value ρ_∞^g set to 0.64 10^{-3} molecule nm^{-3}. Oranges bold lines : best standard Kelvin terms ($\delta_\gamma = 0$) allowing to reproduce the densities to which we add/subtract the density uncertainties. Red bold lines : best interpolation of salty droplet data corresponding to a Tolman length of -0.85 nm, see main manuscript.

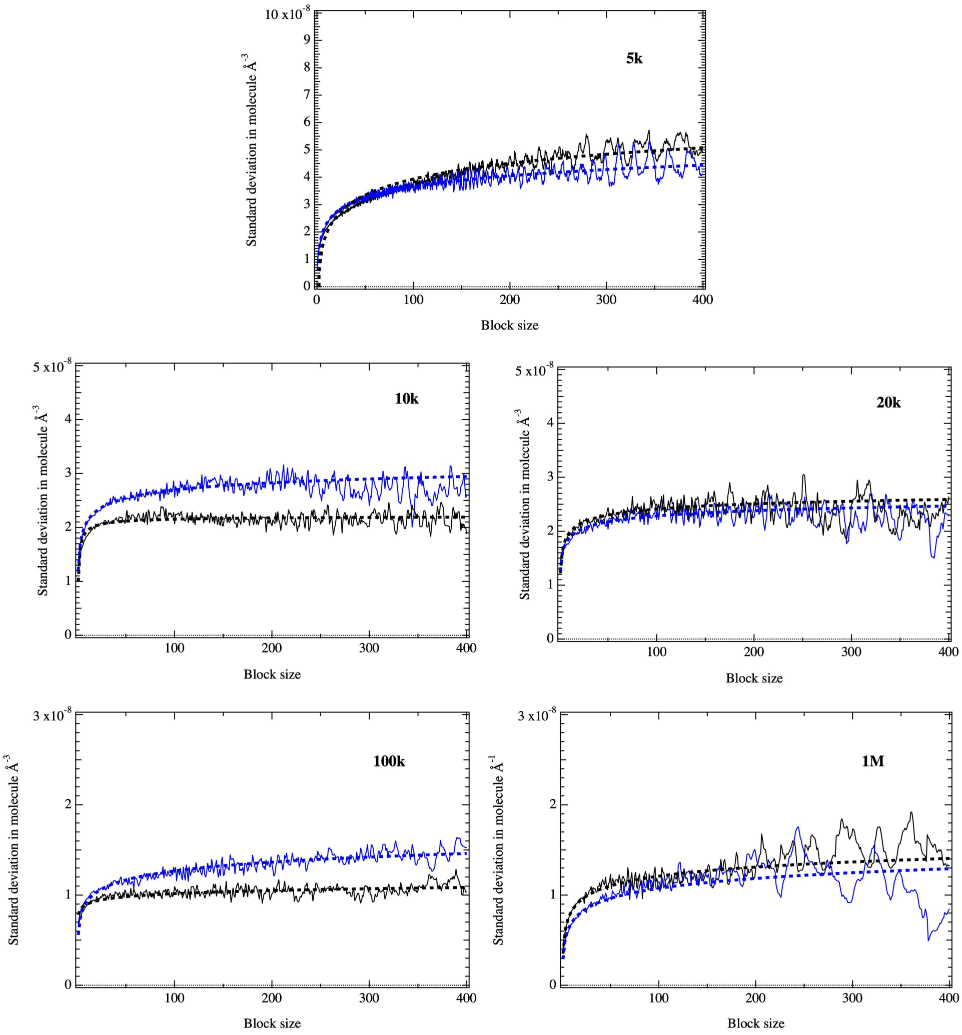

Figure S12: Standard block analysis of the water vapor densities. The density standard deviation values are plotted as a function of the block size b of contiguous temporal data. From up to down : 5k to 1M droplets. Full back and blue lines : 0.2 and 0.6m data. Dashed lines : functions $\alpha + \beta/b^{\gamma}$ whose parameters α, β and γ are adjusted to best reproduce the raw uncertainty data. The upper values of the adjusted parameters α for each kind of 0.2/0.6m droplets are the uncertainties of the mean water vapor density values discussed in the main manuscript, regardless of the salt concentration.

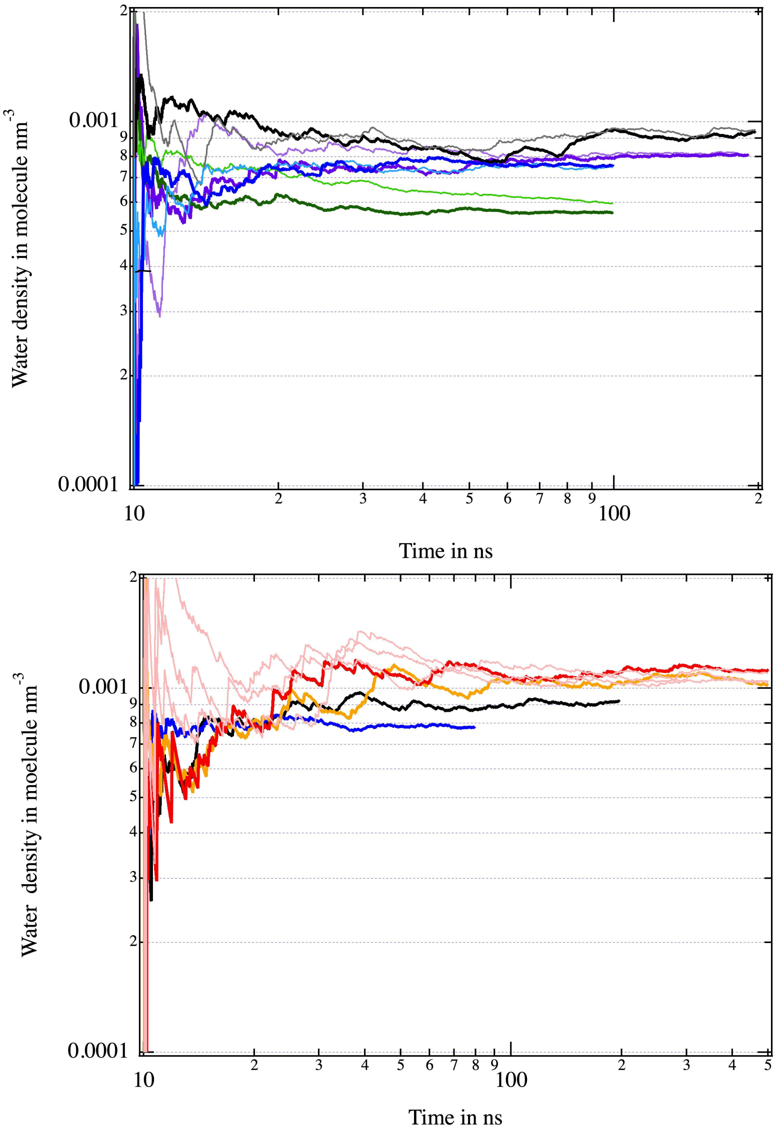

Figure S13: Up : temporal evolutions of the water vapor density for the 0.2m (thin lines) and 0.6m (bold lines) 5k (black), 10k (violet), 20k (blue) and 100k (green) salty droplets. Down : temporal evolutions of the water vapor density for 1k (red bold and thin lines, each line corresponds to an independent 500 ns simulation), 5k (orange), 10k (black) and 20k (blue) pure aqueous droplets.

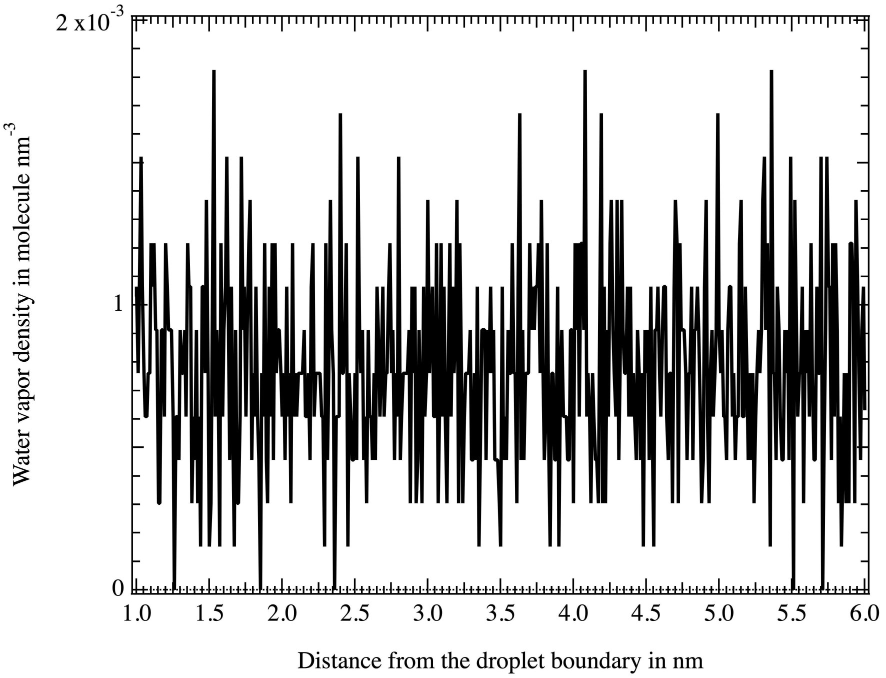

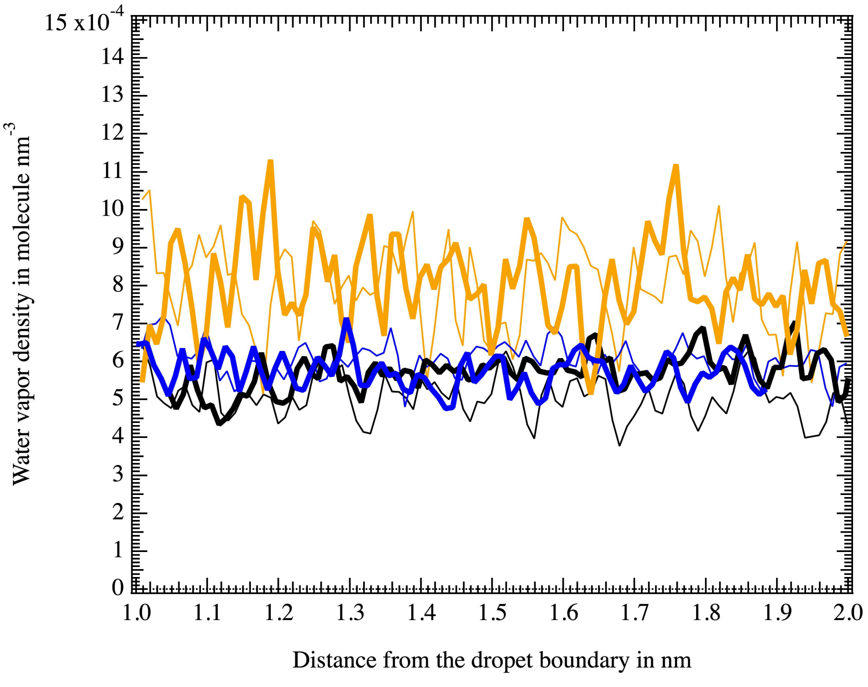

Figure S14: Up : raw mean water vapor density as a function of the distance from the liquid/gas phase planar interface for the 0.2m NaCl aqueous solution as computed along a 100 ns simulation. The vapor density profile for the 0.6m NaCl solution is similar. Down : raw mean water vapor density as a function of the distance from the spherical interfaces of 0.2m (thin lines) and 0.6m (bold lines) NaCl aqueous droplets whose molecular sizes are 10k (orange), 100k (blue) and 1M (black) as computed along our simulations. The densities are averaged on rectangular or spherical shells whose width is set to 0.01 nm.

Tolman length and cumulative number of cloud condensation nuclei

The SSA supersaturation s (in percent) is defined from the Köhler relation according to

$$s = 100 \times \left[1 - \frac{V_{wet} - V_{dry}}{V_{wet} + (1-\kappa)V_{dry}} \times \exp\left(\frac{2\gamma_\infty}{\mathrm{RT}\rho_\infty(R_d + 2\delta_\gamma)}\right)\right]. \qquad (2)$$

$V_{wet} - V_{dry}$ measures the difference in the volumes of a SSA in equilibrium with a water vapor phase (the SSA radius is then R_d) and in its dry state. κ is the SSA hygroscopicity parameter. We set κ to its standard value for NaCl aqueous droplets ($\kappa = 0.67$). For our purpose we set here γ_∞ to the mean value computed for the planar interfaces corresponding to 0.2 and 0.6m NaCl aqueous solutions and we set the water liquid density ρ_∞ to its value for neat water at ambient conditions (33.3 molecule nm^{-3}). In Figure S15 we plot the cumulative numbers of cloud condensation nuclei as a function of the critical supersaturation value s_{crit} (*i.e.* the largest value of s for a SSA corresponding to a dry volume V_{dry}) for a Tolman length set to 0 and of -1 nm. See ref.[5] for details about that kind of plots. For that figure we consider a size (diameter) distribution of SSAs (in their dry state) corresponding to a normalized gaussian centered at 20 nm and which vanishes at 100 nm.

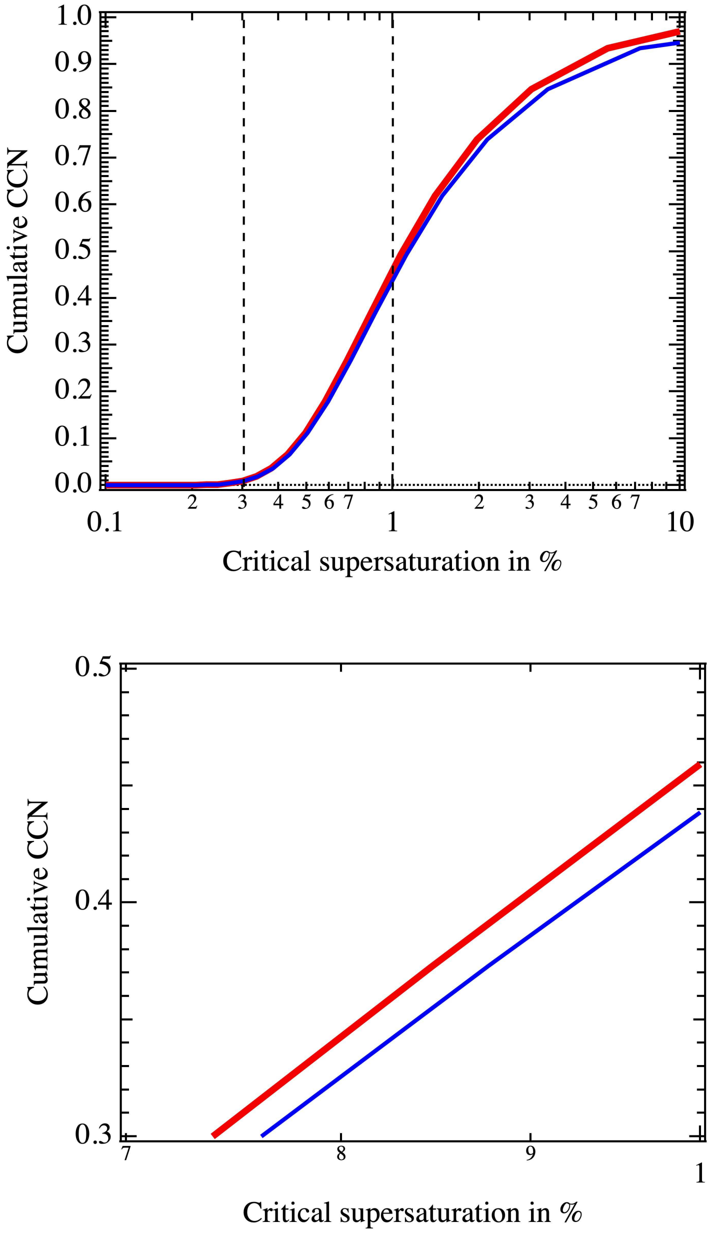

Figure S15: Up : cumulative numbers of CCN for a normalized gaussian distribution of sub-micron NaCl aqueous SSAs as a function of the SSA s_{crit} value for a Tolman length of 0 (red) and of -1 nm (blue). Down : details of the above plots.

References

(1) Réal, F.; Vallet, V.; Masella, M. Improving the Description of Solvent Pairwise Interactions using Local Solute/Solvent Three-Body Functions. The Case of Halides and Carboxylates in Aqueous Environments. *J. Comput. Chem.* **2019**,

40, 1209–1218.

(2) Houriez, C.; Réal, F.; Vallet, V.; Mautner, M.; Masella, M. Ion Hydration Free Energies and Water Surface Potential in Water nano Drops: The Cluster Pair Approximation and the Proton Hydration Gibbs Free Energy in Solution. *J. Chem. Phys.* **2019**, *151*, 174504.

(3) Gloor, G.; Jackson, G.; Bias, F.; de Miguel, E. Test-area simulation method for the direct determination of the interfacial tension of systems with continuous or discontinuous potentials. *J. Chem. Phys.* **2005**, *123*, 134703.

(4) Vega, C.; de Miguel, E. Surface tension of the most popular models of water by using the test-area simulation method. *J. Chem. Phys.* **2007**, *126*, 154707.

(5) Farmer, D. K.; Cappa, C. D.; Kreidenweis, S. M. Atmospheric Processes and Their Controlling Influence on Cloud Condensation Nuclei Activity. *Chem. Rev.* **2015**, *115*, 4199–4217.